AD_____

Award Number: DAMD17-03-1-0095

TITLE: Molecular Engineering of Vector-based Oncolytic and Imaging Approaches for Advanced Prostate Cancer

PRINCIPAL INVESTIGATOR: Lily Wu, M.D., Ph.D.

CONTRACTING ORGANIZATION: University of California, Los Angeles
Los Angeles CA 90024-1406

REPORT DATE: February 2007

TYPE OF REPORT: Final

PREPARED FOR: U.S. Army Medical Research and Materiel Command
Fort Detrick, Maryland 21702-5012

REPORT DOCUMENTATION PAGE

Form Approved
OMB No. 0704-0188

1. REPORT DATE *(DD-MM-YYYY)*	**2. REPORT TYPE**	**3. DATES COVERED** *(From - To)*
01-02-2007	Final	1 FEB 2003 - 31 JAN 2007

4. TITLE AND SUBTITLE

Molecular Engineering of Vector-based Oncolytic and Imaging Approaches for Advanced Prostate Cancer

5a. CONTRACT NUMBER

5b. GRANT NUMBER
DAMD17-03-1-0095

5c. PROGRAM ELEMENT NUMBER

6. AUTHOR(S)
Lily Wu, M.D., Ph.D.

E-Mail: lwu@mednet.ucla.edu

5d. PROJECT NUMBER

5e. TASK NUMBER

5f. WORK UNIT NUMBER

7. PERFORMING ORGANIZATION NAME(S) AND ADDRESS(ES)

University of California, Los Angeles
Los Angeles CA 90024-1406

8. PERFORMING ORGANIZATION REPORT NUMBER

9. SPONSORING / MONITORING AGENCY NAME(S) AND ADDRESS(ES)
U.S. Army Medical Research and Materiel Command
Fort Detrick, Maryland 21702-5012

10. SPONSOR/MONITOR'S ACRONYM(S)

11. SPONSOR/MONITOR'S REPORT NUMBER(S)

12. DISTRIBUTION / AVAILABILITY STATEMENT
Approved for Public Release; Distribution Unlimited

13. SUPPLEMENTARY NOTES

14. ABSTRACT
Hormone refractory and metastatic prostate cancer are not well understood. Better animal models, diagnostic and treatment modalities are sorely needed for these advanced stages of disease. We have developed metastatic prostate cancer animal models that can be monitored by molecular imaging. To target metastatic disease, we have incorporated a highly potent and prostate-specific transcriptional regulatory system (TSTA) in adenoviral vectors such that the expression of imaging reporter gene and therapeutic gene is restricted to prostate cancer cells. Using the prostate-specific TSTA vectors, we were able to map the presence of lymph node metastases by optical or PET imaging. An extension of the TSTA technology is to regulate the expression of viral (E1) replication control gene products such that the lytic viral replicative process is directed at prostate-specific tumor lysis. With extensive molecular engineering, we have demonstrated the feasibility and the functionality of the prostate-targeted oncolytic system. The immediate future plan is to apply the oncolytic viruses in an image-guided oncolytic viral therapy to treat metastatic disease in pre-clinical models of prostate cancer.

15. SUBJECT TERMS
Metastasis, oncolytic adenovirus, gene therapy, imaging

16. SECURITY CLASSIFICATION OF:			**17. LIMITATION OF ABSTRACT**	**18. NUMBER OF PAGES**	**19a. NAME OF RESPONSIBLE PERSON**
a. REPORT	**b. ABSTRACT**	**c. THIS PAGE**			USAMRMC
U	U	U	UU	57	**19b. TELEPHONE NUMBER** *(include area code)*

Table of Contents

Introduction:

The scope of this project is to develop adenoviral vectors that are capable of mediating gene expression specifically in prostate cancer cells. We propose to incorporate a highly potent and specific two-step transcriptional amplification (TSTA) system to mediate prostate-targeted gene expression. In diagnostic applications, this targeted vector will be utilized to express optical and PET imaging reporter genes. The hypothesis is that administration of these imaging reporter vectors could detect prostate metastatic cells in living animals. In a second therapeutic approach, the TSTA system is employed to regulate viral replication, which leads to specific lysis of prostate tumor cells. Creation of consistent and easy to follow metastatic prostate cancer models will be very useful towards the evaluation of the proposed vector-based diagnostic and therapeutic approaches.

Body:

Task 1A: Determine sensitivity of vector-based imaging.

In the last report, we demonstrated that the prostate-targeted adenoviral vector (AdTSTA-sr39tk) can produce robust PET imaging signals in androgen-independent as well as androgen-dependent tumor models by utilizing tissue specific transcriptional amplification (TSTA) system. Two studies have been published from our group demonstrating the prostate-targeted imaging and therapeutic activity of AdTSTA-sr39tk (see below). Based on an earlier publication (Sato et al. Mol Ther 2003) we realized that the activity of the original head-to-head configured TSTA vector can be improved upon. To accomplish this goal, we took on several different approaches (see Figure 1). Instead of locating two components (GAL4VP16 activator and reporter driven by GAL4 binding sites) of the TSTA system as 3'

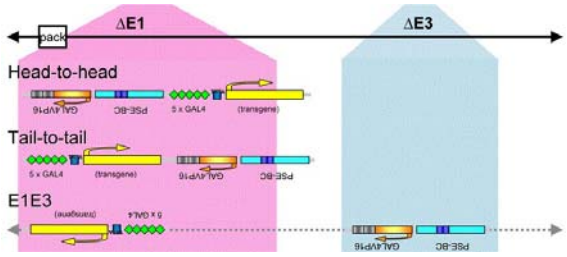

Figure 1. Additional configuration of the TSTA system in adenovirus. In addition to original configuration of the TSTA system (head-to-head), tail-to-tail and E1E3 constructs were created. To make tail-to-tail, both expression cassettes were inverted and inserted in E1 region. The E1E3 was constructed using the plasmid containing activator in E3 region.

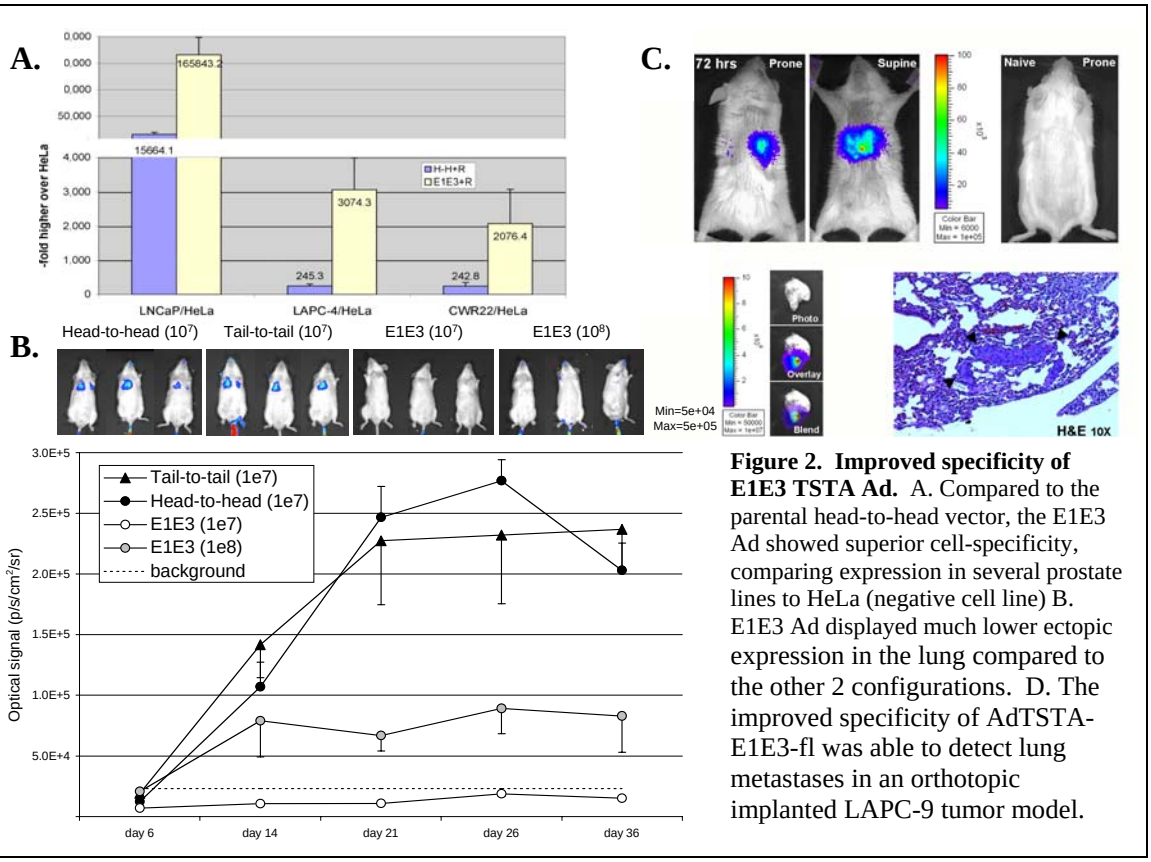

Figure 2. Improved specificity of E1E3 TSTA Ad. A. Compared to the parental head-to-head vector, the E1E3 Ad showed superior cell-specificity, comparing expression in several prostate lines to HeLa (negative cell line) B. E1E3 Ad displayed much lower ectopic expression in the lung compared to the other 2 configurations. D. The improved specificity of AdTSTA-E1E3-fl was able to detect lung metastases in an orthotopic implanted LAPC-9 tumor model.

to 5'-5' to 3' (designated as head-to-head), we developed 5' to 3'-3' to 5' (named tail-to-tail) and one in E1 and another in E3 (named E1E3) (Figure 1). *In vitro* analysis suggested that the E1E3 vector has the higher androgen induction over both head-to-head and tail-to-tail vector (not shown), and it also exhibited superior cell specificity assayed by activity in prostate cancer cell (LNCaP) over non-prostate cell line, HeLa (Figure 2A). In animal studies, the improved selectivity of the E1E3 configured vector was reflected in silenced ectopic expression in the lung. Significantly, the enhanced specificity of the E1E3 vector enabled the detection of lung metastasis of prostate cancer (Figure 2C). This study has been submitted to Gene Therapy (#4 in reportable outcome). The enhanced cell-selectivity of the E1E3 construct is particular pertinent to Task 2, as the designed configuration of our replicating oncolytic construct is similar to the E1E3 vector (see Figure 4).

Task 1B: Imaging metastases in preclinical models.
We have established prostate tumor models that consistently metastasize to regional lymph nodes and lung. As reported last year, these models were induced by expression of pro-lymphangiogenic growth factors (VEGF-C and VEGF-C (C156S) mutant) in the tumor (see Figure 3). These models will greatly facilitate the evaluation of the diagnostic and therapeutic capabilities of our imaging and oncolytic vectors. The first manuscript reporting the lymphatic metastasis models was recently published (#3 in reportable outcome).

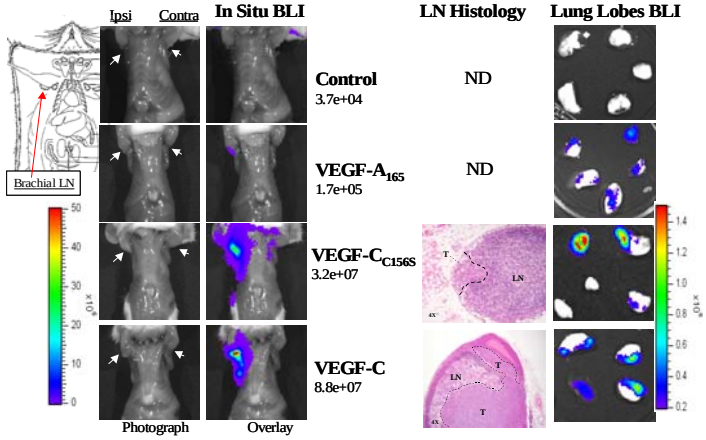

Figure 3. VEGF-C induces LN metastasis. LAPC-9 prostate tumors expressing designated vascular growth factors were grafted in right upper back. Expression of VEGF-C and C156S mutant resulted in metastasis to ipsilateral brachial node (arrow) and lung, confirmed by optical CCD imaging and histology. VEGF-A induces metastasis weakly.

We have applied the TSTA imaging Ad in the lymphatic metastasis models and showed that the vector preferentially traversed to draining lymph nodes, infecting the disseminated tumor cells within the nodes. In doing so, we have developed a specific diagnostic imaging method for nodal metastasis of prostate cancer. This study was submitted and recently accepted in Nature Medicine (#5 in reportable outcome).

Task 1C: Generation of gutless diagnostic Ad, testing in TRAMP model.
We have encounter difficulty in achieving the preset goals of this task for two reasons. 1) The production yield of gutless adenoviral vector is very low, with significant contamination of the helper virus, a first generation adenoviral vector. 2) In our experience, the first generation TSTA diagnostic PET imaging vector is efficient to produce and exhibit high and cell-selective activity (Figure 1 & 2). Thus, we decided to pursue the TSTA vector for further development. Clinical-grade TSTA vector is currently being produced by NCI RAID program for future clinical investigations.

Task 2A: Generation of therapeutic oncolytic adenovirus.
In the last report, we initiated the construction of all-in-one TSTA oncolytic adenovirus after confirming the proper regulated expression in plasmid constructs. The all-in-one TSTA oncolytic adenovirus has E1A and E1B in divergent orientation with centrally located GAL4 binding site repeats (0, 2 or 4) inserted in E1 region and the synthetic transactivator GAL4VP16 regulated by modified PSA promoter inserted in E3 region (Figure 4). As we

shown in Task 1A, superior specificity can be expected with this E1E3 configuration, which should be helpful to safeguard nonspecific viral replication in non-prostate tissues.

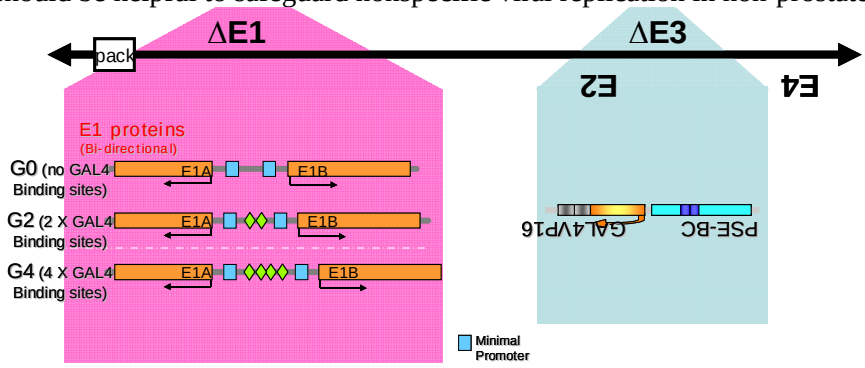

Figure 4. Schematic representation of the all-in-one TSTA oncolytic vectors. Gal4 binding sites, denoted by green diamonds, are situated centrally between divergently transcribed E1A and E1B. The G0 construct serves as a negative control.

Task 2B: In vitro evaluation of TSTA oncolytic adenovirus.
Prostate specific viral DNA replication was observed in *in vitro* infection study using the all-in-one TSTA oncolytic adenovirus with 4 repeats of GAL4 binding sites (AdG4A), which is expected to be the most efficient replicating construct (Figure 5). AdG4A exhibited

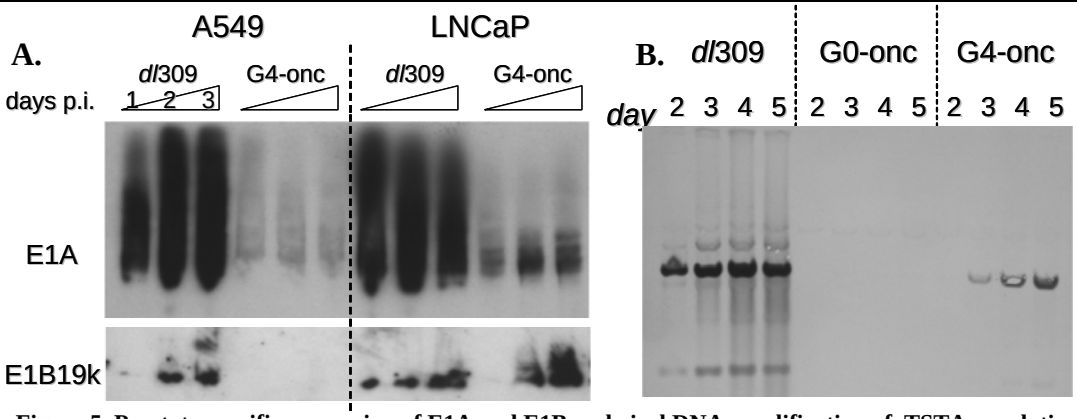

Figure 5. Prostate specific expression of E1A and E1B and viral DNA amplification of TSTA oncolytic adenovirus. A. Lung (A549) or prostate cancer (LNCaP) cell line were infected with increasing titer of wt Ad (dl309) or the TSTA oncolytic adenovirus (AdG4A). E1 proteins were analyzed by western blot at day 2. B. Total DNA was prepared from infected LNCaP cell at specified time points and amplification of viral DNA was confirmed by Southern blot. No DNA amplification was seen for the control G0 oncolytic TSTA Ad.

significant viral DNA replication in LNCaP cells.
The quantitative viral yield of AdG4A as titered by anti-hexon immunoreactivity is significantly (287x) higher than the negative control AdG0A but was 52-fold lower thant wildtype adenovirus (dl309) in LNCaP prostate cancer cell line. However, the replicative

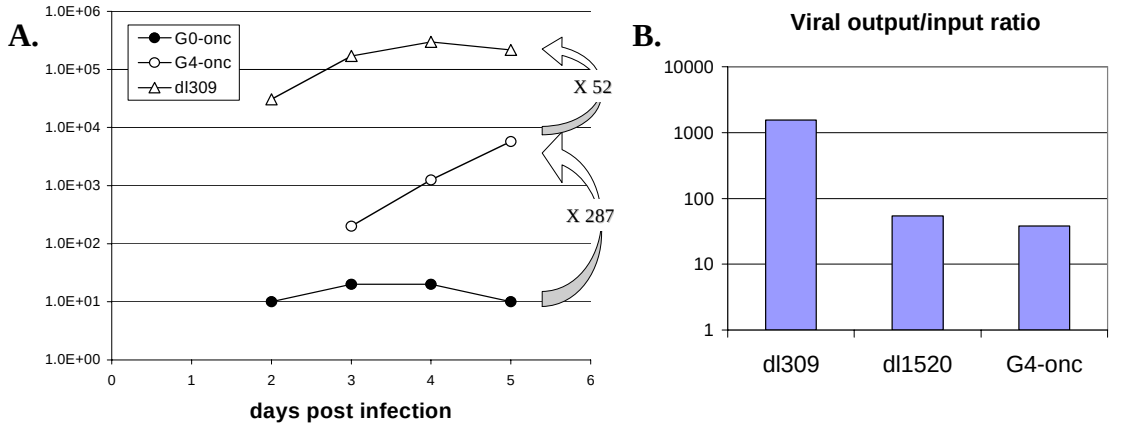

Figure 6. TSTA viral amplification in LNCaP prostate cell lines. A. In LNCaP cell, AdG2A viral expansion was 287 fold higher than AdG0A (control) and it's 52 fold lower than wt dl309 virus. B. The replication efficiency of AdG4A in LNCaP cells is comparable to the E1B-deleted dl1520 (Onyx-015), but is significantly lowered than dl309.

activity of AdG4A is comparable to another cancer-selective oncolytic virus dl1520 (Onyx-015) (Figure 6). The tumoricidal therapeutic activity of AdG4A was analyzed in cell culture (Figure 7). TSTA oncolytic adenovirus with 2 GAL4 binding sites (AdG2A) was used in this experiment as an ineffective replicating control virus. As shown in Figure 7, androgen-dependent LNCaP and LAPC-4 cell are more susceptible to viral oncolysis than androgen-independent CWR22rv1 and A549 (lung carcinoma). AdG4A oncolytic virus was able to mediate effective cytopathic effects on LNCaP cells in comparison to a replication-deficient CMV-luciferase virus and AdG2A. Collectively, these preliminary findings indicate that AdG4A is able to selectively replicate and induce cytotoxicity in prostate tumor cells. However, the kinetic of viral replication appear to be delayed compared to wildtype virus (dl309) and the magnitude of burst is reduced compared to dl309 but comparable to dl1520.

Task 3C: In vivo analyses of therapeutic activity of oncolytic virus.
Currently, we are actively analyzing the therapeutic activity of AdG4A in preclinical prostate tumor models, including the lymphatic metastasis models described above. We anticipate to complete the in vivo experiments and the manuscript within the next 6 months.

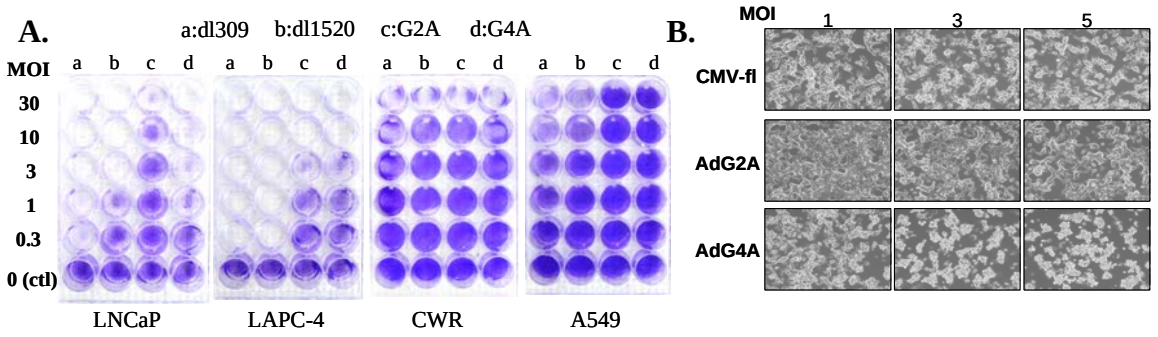

Figure 7. Oncolytic activity in prostate cancer cells. A. Different cell lines were infected with increasing MOI of 4 oncolytic virus dl309 (wt, a); dl1520 (E1B-deleted tumor selective Ad, b); G2A (control, c); G4A (prostate-specific TSTA oncolytic Ad, d). Amount of viable tumor cells were reflected by the crystal violet staining at 4 days after infection. B. Cytopathic effects can be observed more prominently in the AdG4A infected cell than the other control virus (AdCMV-fl and AdG2A).

Key Research Accomplishments:

- We demonstrated that different configurations of prostate-specific TSTA adenoviral vector that exhibited superior specificity and androgen responsiveness than the original head-to-head configuration. This improved configuration has been incorporated into our oncolytic virus.
- Image-guided gene therapy was achieved with TSTA adenoviral vectors in pre-clinical model of hormone refractory prostate cancer.
- We have developed lymphatic metastasis model of prostate cancer that can be monitored by molecular imaging. These models will be very useful in the development of vector-targeted diagnostic imaging.
- The all-in-one TSTA oncolytic adenovirus (AdG4A) has been constructed and their ability to target prostate cancer was demonstrated. The analyses of its therapeutic activity are nearly complete.

Reportable Outcomes (cumulative over the entire grant period)**:**

Manuscripts:

1) Sato M, Johnson M, Zhang L, Gambhir SS, Carey M, Wu L. Functionality of Androgen Receptor-based Gene Expression Imaging in Hormone Refractory Prostate Cancer. Clin Can Res 2005, 11:3743-9.

(This study confirms that modified PSA promoter (PSE-BC) mediated TSTA adenoviral vector can direct effective gene expression including PET imaging reporter gene in androgen-independent prostate tumor.)

2) Johnson M, Sato M, Burton J, Gambhir SS, Carey M, Wu L. MicroPET/CT monitoring of herpes thymidine kinase suicide gene therapy in a prostate cancer xenograft: the advantage of a cell-specific transcriptional targeting approach. 2005 Mol Imaging, 4:463-72.

(This study utilized TSTA adenovirus expressing HSV-tk gene in cytotoxic gene therapy that's coupled to molecular imaging.)

3) Brakenhielm E, Burton JB, Johnson M, Chavarria N, Morizono K, Chen I, Alitalo K, Wu L. Modulating metastasis by a lymphangiogenic switch in prostate cancer. Int J Can 2007 121:2153–2161. (featured on journal cover)

(This study applied optical imaging to monitor lymphatic metastasis in a mouse model of prostate cancer.)

4) Sato M, Figueiredo ML, Burton JB, Johnson M, Chen M, Powell R, Gambhir SS, Carey M, Wu L. Configurations of a Two-Tiered Amplified Gene Expression System in Adenoviral Vectors Designed to Improve the Specificity of In Vivo Prostate Cancer Imaging, in submission, Gene Ther (2007)

(This study describes the improved configurations of TSTA adenoviral vectors.)

5) Burton JB, Johnson M, Sato M, Koh SB, Stout S, Mulholland D, Chatziioannou AF, Phelps M, Wu H. Wu L. Adenovirus Mediated Gene Expression Imaging to Directly Detect Sentinel Lymph Node Metastasis of Prostate Cancer, Nat Med (2008), in press.

(This study employs the AdTSTA-fl and AdTSTA-sr39tk in a novel biomarker-based lymphangiography to specifically image nodal metastasis of prostate cancer. Manuscript enclosed in appendix)

Conclusions:

We have demonstrated that the TSTA approach can greatly augment prostate-specific gene expression, and the TSTA adenoviral vectors can mediate effective imaging and therapeutic activity in animal prostate tumor models. We have developed several lymphatic metastatic prostate cancer models and demonstrated that the prostate-targeted TSTA imaging vectors are able to mediate effective gene transfer and specifically detect the presence of nodal metastases. The feasibility and functionality of prostate-specific oncolytic adenovirus regulated by the bi-directional TSTA method have been demonstrated. The evaluation of the TSTA oncolytic virus mediated therapeutic strategy in advanced androgen-independent and metastatic stage of disease are underway.

Appendices:

Published work:

1) Brakenhielm E, Burton JB, Johnson M, Chavarria N, Morizono K, Chen I, Alitalo K, Wu L. Modulating metastasis by a lymphangiogenic switch in prostate cancer. Int J Can 2007 121:2153–2161.

Manuscript in press:

2) Burton JB, Johnson M, Sato M, Koh SB, Stout D, Mulholland D, Chatziioannou AF, Phelps M, Wu H. Wu L. Adenovirus Mediated Gene Expression Imaging to Directly Detect Sentinel Lymph Node Metastasis of Prostate Cancer, Nat Med (2008), in press.

Int. J. Cancer: **121,** 2153–2161 (2007)

Modulating metastasis by a lymphangiogenic switch in prostate cancer

Ebba Brakenhielm[1], Jeremy B. Burton[2], Mai Johnson[2], Nelson Chavarria[1], Kouki Morizono[3], Irvin Chen[3], Kari Alitalo[4] and Lily Wu[1,2,5]*

[1]*Department of Urology, David Geffen School of Medicine at UCLA, Los Angeles, CA*
[2]*Department of Molecular & Medical Pharmacology, David Geffen School of Medicine at UCLA, Los Angeles, CA*
[3]*Department of Microbiology, Immunology and Molecular Genetics, David Geffen School of Medicine at UCLA, Los Angeles, CA*
[4]*Molecular/Cancer Biology Laboratory and Ludwig Institute for Cancer Research, Helsinki University Central Hospital, Helsinki, Finland*
[5]*Crump Institute of Molecular Imaging, David Geffen School of Medicine at UCLA, Los Angeles, CA*

Prostate cancer dissemination is difficult to detect in the clinic, and few treatment options exist for patients with advanced-stage disease. Our aim was to investigate the role of tumor lymphangiogenesis during metastasis. Further, we implemented a noninvasive molecular imaging technique to facilitate the assessment of the metastatic process. The metastatic potentials of several human prostate cancer xenograft models, LAPC-4, LAPC-9, PC3 and CWR22Rv-1 were compared. The cells were labeled with luciferase, a bioluminescence imaging reporter gene, to enable optical imaging. After tumor implantation the animals were examined weekly during several months for the appearance of metastases. Metastatic lesions were confirmed by immunohistochemistry. Additionally, the angiogenic and lymphangiogenic profiles of the tumors were characterized. To confirm the role of lymphangiogenesis in mediating metastasis, the low-metastatic LAPC-9 tumor cells were engineered to overexpress VEGF-C, and the development of metastases was evaluated. Our results show CWR22Rv-1 and PC3 tumor cell lines to be more metastatic than LAPC-4, which in turn disseminates more readily than LAPC-9. The difference in metastatic potential correlated with the endogenous production levels of lymphangiogenic growth factor VEGF-C and the presence of tumor lymphatics. In agreement, induced overexpression of VEGF-C in LAPC-9 enhanced tumor lymphangiogenesis leading to the development of metastatic lesions. Taken together, our studies, based on a molecular imaging approach for semiquantitative detection of micrometastases, point to an important role of tumor lymphatics in the metastatic process of human prostate cancer. In particular, VEGF-C seems to play a key role in prostate cancer metastasis.

Key words: lymphatics; vascular endothelial growth factor; lung; luciferase; lymph node

Prostate cancer affects 1 out of every 6th man in the U.S.[1] Already at first diagnosis about 20–30% of patients present with advanced stage disease, for which the therapeutic approaches include radical prostate surgery and hormone ablation. This group of patients is at increased risk of tumor progression after therapy, through the development of androgen-independent disease and metastasis, for which there currently is no effective treatment. During 2006 prostate cancer was estimated to claim around 30,000 lives,[1] making it the second most common cause of cancer mortality in men.

Metastasis is a multistep process where tumor cell dissemination to distal sites occurs through the blood or lymphatic system. Lymph nodes, together with bone and liver, represent the most common sites of metastasis in prostate cancer. For example, pelvic lymph node metastases have been reported in 50–60% of advanced-grade prostate cancer patients,[2–4] and is considered as the strongest predictor of disease recurrence and progression.[5–7] Further, the risk of dying from prostate cancer within 5 years after radical prostatectomy is increased up to 6-fold depending on the degree of lymph node involvement.[8] Thus, the lymphatic vasculature may be the most common path for dissemination in prostate cancer similar to in breast cancer.[9,10] Tumor cells may gain access to the lymphatic circulation either *via* migration towards pre-existing lymph vessels or by stimulation of lymphatic sprouting into the tumor through secretion of lymphangiogenic growth factors.[11,12] In recent years, the complex regulation of lymphangiogenesis has begun to unravel, through the discovery of specific markers for lymphatic endothelial cells and their selective growth factors and receptors.[13] Many clinical studies have found that elevated lymphangiogenic growth factor expression in the tumor, the presence of tumor lymphatics and/or lymph node micrometastases correlate with poor prognosis and distal organ metastasis.[11] The best studied example is breast cancer, where clinical assessment of sentinel lymph node involvement is becoming the standard for diagnosis, prognosis and therapeutic guidance. For prostate cancer, several clinical studies have similarly shown correlations between elevated lymphangiogenic growth factor expression in the tumor and lymph node metastasis and advanced-stage disease.[14–17] Despite these indications, only recently have some experimental data emerged concerning the occurrence of lymphangiogenesis in animal models of prostate cancer,[18,19] thus highlighting the need for further studies to delineate the role of the lymphatic system to guide the development of novel tools for prevention and treatment of prostate cancer metastasis.

In our study we have investigated the impact of tumor lymphangiogenesis on prostate cancer metastasis. We first examined and compared the metastatic potential of 2 recent xenograft models of human prostate cancer, LAPC-4 and LAPC-9.[20,21] These models recapitulate many characteristics of the human disease: (*i*) the tumor cells express *wt* androgen receptor, (*ii*) the tumor growth is relatively slow and androgen-dependent, (*iii*) the tumor cells express prostate specific antigen (PSA). Additionally, we compared the metastatic tendencies and vascular growth factor expression levels of these 2 models to the highly aggressive prostate cancer cell lines CWR22Rv-1 and PC3. Further, to directly query the causative role of tumor lymphangiogenesis in mediating tumor metastasis we evaluated the influence of overexpression of the lymphangiogenic growth factor VEGF-C on metastasis in the weakly metastatic LAPC-9 tumor model. These respective goals were achieved by a noninvasive optical bioluminescence imaging approach that enabled us to monitor the development of distant

Abbreviations: FL, firefly luciferase; LYVE-1, lymph vessel endothelial hyaluronan receptor-1; MOI, multiplicity of infection; PSA, prostate specific antigen; ROI, region of interest; RL, renilla luciferase; SCID, severe combined immune-deficient; VEGF-A, vascular endothelial growth factor-A; VEGF-C, vascular endothelial growth factor-C; VEGFR-3, vascular endothelial growth factor receptor-3.

The first two authors contributed equally to this work.

Grant sponsor: NCI SPORE program; Grant number: P50 CA092131; Grant sponsor: California Cancer Research Program; Grant number: 3NI0226; Grant sponsor: UCLA RTPS Training program; Grant number: No. T32-GM008652; Grant sponsor: Swedish Wenner-Gren Foundations.

***Correspondence to:** Department of Urology, MRL 2210, Box 951738, University of California, Los Angeles, CA 90095-1738, USA.
Fax: +310-206-5343. E-mail: lwu@mednet.ucla.edu

Received 3 November 2006; Accepted after revision 2 April 2007
DOI 10.1002/ijc.22900
Published online 21 June 2007 in Wiley InterScience (www.interscience.wiley.com).

metastasis in real-time and to locate and quantify micrometastatic lesions in isolated tissues.[22,23] We show here that lymphangiogenesis and VEGF-C expression correlated with lymph node and lung metastasis in the 4 different prostate cancer cell lines examined. Further, we demonstrate that overexpression of VEGF-C resulted in the stimulation of tumor lymphangiogenesis generating a switch from a low-metastatic to a highly-metastatic tumor.

Material and methods

All handling of animals was performed in accordance with the University of California, Los Angeles (UCLA) Animal Research Committee guidelines. Prostate epithelial cell basal medium (PrEBM) and Bulletpack supplements were obtained from Clonetics (San Diego, CA).

Tumor cells

The androgen-dependent human prostate cancer cell lines, LAPC-4 and LAPC-9, derived as previously described,[20,21,24] were kind gifts from Dr. Charles Sawyers (UCLA, Los Angeles, CA). The cells were maintained by *in vivo* passage as subcutaneous xenograft tumors in male severe combined immune-deficient (scid) natural killer cell knock-out ($NK^{-/-}$) mice (Taconic farms; Germantown, NY). During *in vitro* manipulations these cells were seeded in PrEBM supplemented with bovine pituitary extract, insulin, hydrocortisone, GA-1000, retinoic acid, transferrin, T_3, epinephrine and human EGF (Bulletpack, Clonetics). The tumor cells were reimplanted within 3 days of *in vitro* culture. The CWR22Rv-1 and PC3 tumor cell lines (kind gifts from Dr. David Agus, Cedars-Sinai Medical Center, Los Angeles, CA) were maintained *in vitro* in RPMI and DMEM, respectively, containing 10% FBS and 1% Penicillin/Streptomycin.

Lentiviral production and tumor transduction

Before each experiment, fresh LAPC-4 and LAPC-9 tumor tissues were collected to prepare single cell suspensions. Tumor cells were transduced using lentivirus carrying CMV promoter-driven firefly luciferase (FL) or renilla luciferase (RL) reporter genes, as previously described.[25] Briefly, the luciferase genes were subcloned from phFL-cmv or phRL-cmv (Promega, Madison, WI) plasmids and inserted downstream of the hCMV promoter in the pCCL-M4 lentiviral vector,[26] resulting in the pCCL-cmv-luciferase-M4 vector used to generate LAPC-4-cmv-FL (hereafter referred to as LAPC-4), LAPC-9-cmv-FL (LAPC-9), LAPC-9-cmv-RL, CWR22Rv-1-cmv-RL (CWR22Rv1) and PC3-cmv-RL (PC3). In a second experiment, LAPC-9 tumors expressing RL were transduced in suspension with lentiviral vector pCCL-VEGFC-IRES-eGFP (LAPC-9/VEGF-C) or empty vector control pCCL-IRES-eGFP (LAPC-9/GFP). Recombinant lentivirus was produced by calcium phosphate cotransfection of 293T cells. Tumor cells were infected using viral supernatant at MOI 1 or 2 during 4 hr of incubation. Robust and constitutive cellular expression of luciferase enzymes were confirmed by an *in vitro* bioluminescence assay (Promega).

In vivo *and* ex vivo *optical imaging of primary tumor growth and metastasis*

One million lentiviral-transduced tumor cells (LAPC-4, LAPC-9, LAPC-9/GFP, LAPC-9/VEGF-C, CWR22Rv-1 or PC3) expressing FL or RL reporter genes were subcutaneously implanted in the right upper back of immune-deficient male scid/$nk^{-/-}$ mice ($n = 6$–10). Tumor sizes were measured regularly using digital calipers. After administration of luciferase substrates (D-luciferin, 150 mg/kg i.p. for FL; coelenterazine, 1 mg/kg i.v. for RL) the anaesthetized mice were imaged using the bioluminescence optical imager (IVIS 200; Xenogen, Alameda, CA) immediately after tumor implantation and weekly thereafter according to previously described techniques.[22,27] Maximal luciferase signals were semiquantified using Living Image 2.5 (Xenogen) and IGOR (Wavemetrics, Lake Oswego, OR) image analysis softwares. Bioluminescence *in vivo* signal was considered positive if the signal in the region of interest (ROI) exceeded 1×10^5 photons/sec/cm^2/steradian (p/s/cm^2/sr).

The primary tumors were grown to the ethical limit of 15 mm in diameter, at which time the animals either were sacrificed or the tumors surgically removed, as indicated. After operation, the mice were analyzed weekly by optical imaging to monitor the occurrence of metastases. The mice were sacrificed within 100 days postoperation or earlier if either primary tumors regrew or other adversary health signs developed. Upon sacrifice of all animals, the whole body and free-dissected organs were imaged *ex vivo* for bioluminescence after a brief application of luciferase substrate. Data are reported as the average of maximal bioluminescent signals in the ROI and in the unit of p/s/cm^2/sr.

Immunohistochemistry

Tumors, lungs and lymph nodes were processed for histological examination ($n = 6$–9). Paraffin-embedded sections (5 μm) were stained for a vascular endothelial marker (biotinylated rat anti-mouse CD31 1:100, BD Biosciences, San Jose, CA), lymphatic endothelial markers (rabbit anti-LYVE-1 1:300, RELIATech, Braunschweig, Germany; rabbit anti-Prox1, 1:100, Novus Biologicals, Littleton, CO; and rabbit anti-VEGF receptor (VEGF R)-3, 1:200, Santa Cruz Biotechnology, Santa Cruz, CA), a macrophage marker (rat anti-F4/80, 1:100, AbD Serotech, Raleigh, NC), or a prostate epithelial marker (mouse anti-human pan cytokeratin 1×, Biogenex, San Ramon, CA) as previously described.[28] HRP-conjugated secondary reagents (Vector Laboratories, Burlingame, CA) were detected either using the chromogen diaminobenzidine or fluorescent conjugates (NEN TSA kits, Perkin Elmer, Boston, MA). Confocal microscopic images were taken at 10× or 20× optical magnification using a Carl Zeiss LSM 310 Laser Scanning Confocal microscope.

Images were processed using Photoshop software (Adobe systems, San Jose, CA). For each histological analysis 6–9 animals were included with 5–20 micrographs per animal. Blood or lymphatic vessel profiles (vascular density and vessel lumen sizes) were analyzed in pictures at 10× or 20× optical magnification using a stereological approach as previously described.[29] Briefly, blood vessels were analyzed in sections stained with CD31 and lymphatic vessels were analyzed in sections double labeled for CD31 and LYVE-1 to discriminate between blood and lymphatic vessels. Lymphatic vessels within the tumor and close to the peripheral tumor border were classified as intratumoral vessels, whereas LYVE-1 positive structures outside the tumor border were classified a peritumoral lymphatics.

Real time RT-PCR

Fresh tumor tissue was snap frozen in liquid nitrogen, and stored at −80°C until analysis. The tissue was ground to a fine powder in liquid nitrogen and RNA was extracted using Tri-reagent (Sigma-Aldrich, St Louis, MO) according to the manufacturer's suggested protocol. RNA (1 μg) was reverse transcribed by incubation for 1 cycle at 25°C for 10 min, 48°C for 45 min and 95°C for 5 min. Reaction conditions were as follows: 1× RT-buffer, 5.5 mM $MgCl_2$, 500 μM dNTP, 2.5 μM random hexamer primer, 0.4 U/μl RNase inhibitor and 1.25 U/μl reverse transcriptase enzyme. For each sample, 1 μl cDNA (∼ 20 ng) was amplified using SyBr green 2× master mix (Applied Biosystems, Foster City, CA) and 10 μM of the following primers:

Actin:
- forward 5′ TCAAGATCATTGCTCCTCCTGAGC 3′
- reverse 5′ TACTCCTGCTTGCTGATCCACATC 3′

hVEGF-C:
- forward 5′ CGGCTTATGCAAGCAAAGATCTGG 3′
- reverse 5′ GCCTCCTTTCCTTAGCTGACACTT 3′

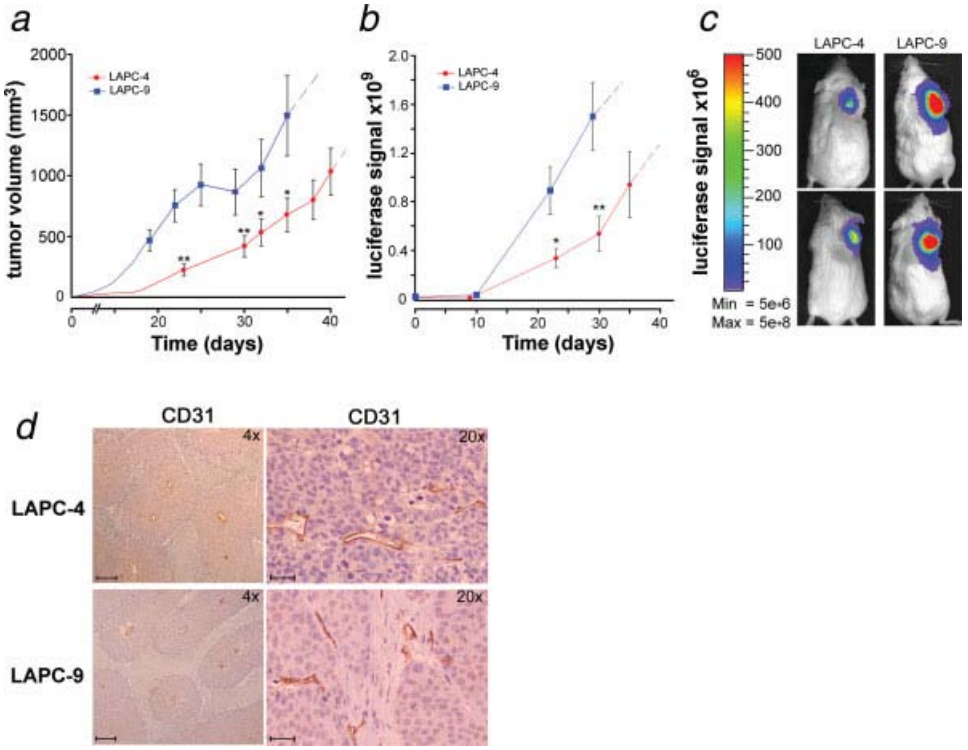

FIGURE 1 – Prostate cancer xenograft models: optical imaging of tumor growth. LAPC-4 and LAPC-9 human tumor cells were implanted in immune-deficient mice ($n = 10$). Tumor volume was measured (*a*) and the luciferase reporter gene (FL) activity assayed *via in vivo* optical imaging (*b*). Blue color = LAPC-9 group; red color = LAPC-4 group. Dashed extensions of the curves represent projected values after tumors had been surgically removed in the majority of animals in a group. Representative examples of the tumor-derived optical signal in LAPC-4- and LAPC-9-bearing mice at day 20 postimplantation are shown (*c*). The color bar indicates the intensity range of the bioluminescence signal (p/s/cm^2/sr). The tumors were surgically removed within 4–7 weeks postimplantation. Immunohistochemical staining of blood vessels in tumor sections revealed no difference in vascularity between the groups (*d*; ×4 and ×20). Scale bars = 200 and 50 μm, respectively.

hVEGF-A:

- forward 5′ AGGAGTACCCTGATGAGATCGAGT 3′
- reverse 5′ CATGGTGATGTTGGACTCCTCAGT 3′

The reaction was run on an Opticon Monitor 2 real time PCR machine (MJ Research/Biorad, Waltham, MA). Samples were amplified using Opticon Monitor 2 real time technology under the following cycling conditions: 39 cycles of 95°C/15 sec, 60°C/30 sec and 72°C/30 sec. Gene expression was determined by standard curve method and normalized to β-actin expression ($n = 4$ tumors per group).

Statistical analysis

Student's two-tailed *t*-test was used to calculate statistical differences between 2 groups. $p < 0.05$ was considered significant.

Results

Characterization of the LAPC-4 and LAPC-9 wt *tumors*

One million LAPC-4 or LAPC-9 tumor cells overexpressing FL were implanted in the right upper back of immune-deficient mice. The expression level of FL was similar in both tumor cell lines, at 5–7 × 10^5 relative light units/s/μg protein as measured *in vitro* prior to implantation. The animals were investigated using bioluminescence imaging immediately after implantation and weekly thereafter. The LAPC-4 tumors established at a slightly slower rate than the LAPC-9 tumors (Fig. 1*a*). The tumor growth was mirrored by an exponential increase in the emitted *in vivo* luciferase signal (Figs. 1*b* and 1*c*). Tumors were surgically removed when they reached the upper ethical limit. The *in vivo* optical signal from the primary tumors at the time of resection was between 1.1–1.4 × 10^9 p/s/cm^2/sr, and the sizes of the removed tumors were similar in both groups (data not shown). Detailed immunohistochemical analysis revealed that there were no differences in the degree of vascularity between LAPC-4 and LAPC-9 tumors, as determined by the evaluation of both vessel numbers and vessel sizes (Fig. 1*d*, data not shown).

In vivo *and* ex vivo *optical monitoring of the development of metastases*

Because of light scattering properties *in vivo*, low-intensity bioluminescence emitted from micrometastatic lesions may be difficult to detect in the presence of a strong bioluminescence signal produced by primary tumors.[30] Thus, the surgical resection of primary tumors performed in our study not only mimics therapeutic intervention in the clinic but also removes the intense bioluminescence focus thus enabling sensitive monitoring of metastasis development *in vivo*. Immediately after primary tumor removal no signs of secondary lesions were observed. However, within 3 weeks some mice in the LAPC-4 group showed significant optical signals emitted from the ventral side, in a position suggestive of lung metastasis. The further development and growth of these potential metastatic lesions was monitored up to 100 days after the primary tumor removal or until adversary health signs developed (Figs. 2*a* and 2*c*). During this time, 7 out of 9 mice in the LAPC-4 group acquired strong luciferase signals in locations distant from the primary tumor implantation site. No such *in vivo* imaging signals were found in the LAPC-9-implanted mice (Figs. 2*b* and 2*c*). Tumor regrowth in the surgical site occurred in 5 out of 7 (71%) LAPC-9 mice and in 4 out of 9 (44%) LAPC-4-implanted mice. Thus animals were evaluated at sacrifice to confirm the specific location of metastases by *ex vivo* imaging of dissected organs. In the LAPC-4 group 100% (9 out of 9) of the animals had developed optically detectable metastatic lesions, primarily in lung and regional lymph nodes (Table I, Figs. 2*d* and 2*e*), with an average *ex vivo* lung metastatic signal intensity of 3.9 × 10^7 p/s/cm^2/sr. In contrast, optical signs of metastases could only be found in less than 29% (2 out of 7) of LAPC-9-implanted mice, where positive signals were observed in 1 lung and in 1 brachial lymph node, respectively (Table I, Fig. 2*f*). Furthermore, these signals were comparably weaker; at less than 12% of the optical intensity observed in LAPC-4-implanted mice.

Immunohistochemical analyses of primary tumors and metastases

To confirm the metastatic lesions identified by optical imaging, the lungs and lymph nodes were retrieved for immunohistochemi-

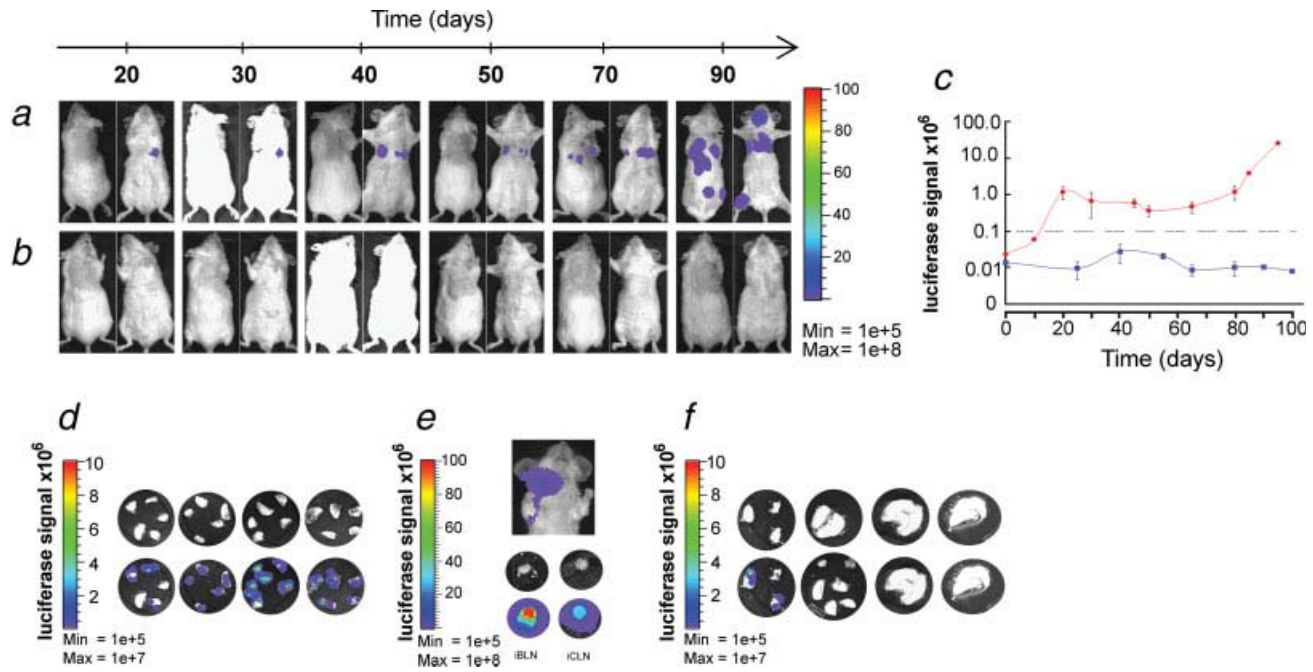

FIGURE 2 – Tumor metastasis monitored by *in vivo* and *ex vivo* optical imaging. Representative examples of dorsal and ventral optical images of mice in the LAPC-4- (*a*) and LAPC-9 cohort (*b*) at various time points following primary tumor resection are shown. The appearance of bioluminescence signal above background was first evident in the ventral side of the mice, suggestive of lung metastases. The color bar to the right indicates the signal intensity range (p/s/cm^2/sr $\times$ 10^6). The maximal luciferase signal emitted from the ventral side of animals in LAPC-4- and LAPC-9 groups is plotted over time after tumor removal (*c*). The grey dashed line shows the level set for background signal. Only LAPC-4-implanted mice developed *in vivo* signals indicative of metastasis. These secondary sources of bioluminescence emission in the animals remained stable or increased in intensity over time. Blue color = LAPC-9 group; red color = LAPC-4 group. Data represent averages ±SEM (n = 4). Within 100 days after the tumor removal the animals were sacrificed and the lungs and lymph nodes dissected and imaged optically for the presence of tumor cell-derived luciferase signal. Lung metastatic signs were observed in all but one of the LAPC-4- (n = 9) and in only one of the LAPC-9-implanted mice (n = 7), whereas lymph node signals were found in three LAPC-4 mice and in one LAPC-9 mouse (see Table I). Representative examples of lungs (*d*) and lymph nodes (*e*) from the LAPC-4 group and lungs (*f*) from the LAPC-9 group are shown. The color scale indicates bioluminescence intensity (p/s/cm^2/sr). The upper row circular microphotographs are each from a different animal, and the lower row pictures are the corresponding bioluminescence composite images. iBLN, ipsilateral brachial lymph node; iCLN, ipsilateral cervical lymph node.

cal analyses. Both LAPC-4 and LAPC-9 tumor cells could be easily distinguished using human cytokeratin as a marker, as seen by the intense cytoplasmic staining in the primary tumors (Fig. 3*a*). Lymph nodes from the LAPC-4 group with positive optical signals were found to contain tumor masses involving up to 50% of the nodal area in brachial or cervical lymph nodes (Fig. 3*b*). Similarly, the tumor cells present in the lung stained strongly for cytokeratin, making identification of metastases straightforward (Fig. 3*c*). Multiple metastatic lesions were found in lungs from the LAPC-4 group, confirming the results of the optical imaging (Fig. 3*d*). The 1 LAPC-9 animal with optical signal emitted from the lungs was also verified to carry lung metastases, whereas all other lungs of the LAPC-9 cohort were negative (data not shown).

TABLE I – NUMBER OF MICE WITH LUCIFERASE POSITIVE LUNGS OR LYMPH NODES (LN) AT SACRIFICE AS JUDGED BY *EX VIVO* OPTICAL IMAGING

Degree of involvement	LAPC-4	LAPC-9
Lungs		
No metastasis	1	6
1–2 Positive lobes	2	0
3–4 Positive lobes	1	1
All lung lobes positive	5	0
Incidence of lung metastasis	**89%**	**14%**
Lymph nodes		
No metastasis	6	6
Positive brachial LNs	2	1
Positive cervical LNs	3	0
Incidence of LN metastasis	**33%**	**14%**

In the LAPC-4 implanted mice 2 out of 9 mice had both brachial and cervical lymph node metastases. The total number of animals with luciferase positive lymph nodes in the LAPC-4 group was 3 animals.

Evaluation of the angiogenic and lymphangiogenic profiles of the primary tumors

To investigate the presence of tumor lymphatics immunohistochemical analyses were performed on paraffin-embedded primary tumor sections. Samples were double stained to visualize blood and lymph vessels simultaneously. In LAPC-4 tumors, LYVE-1-positive structures were present in the tumor periphery, and thin lymphatic vessels were found penetrating into the tumor, often alongside clusters of blood vessels (Figs. 3*e* and 3*f*). The lymphatic nature of these structures was confirmed by staining for murine VEGFR-3 (Fig. 3*g*). In contrast, LAPC-9 tumors were generally lacking intratumoral lymphatics, except for occasional small lymph vessels close to the tumor border (Figs. 3*e* and 4*d*).

To determine if the observed differences in tumor lymphatics were due to differences in vascular growth factor expressions, real time RT-PCR analyses were performed. LAPC-4 tumors showed a slight 1.6-fold increase in vascular endothelial growth factor (VEGF)-A expression levels as compared to LAPC-9 tumors, although it did not reach significance (Fig. 3*h*). This is in line with our finding that these tumors were equally vascularized. In contrast, the expression of the lymphangiogenic factor VEGF-C was significantly elevated in LAPC-4, at 3.3-fold higher levels as compared to LAPC-9 (p = 0.01, Fig. 3*h*), in agreement with the tumor lymphatics results earlier. The difference in VEGF-C expression levels in LAPC-4 compared to LAPC-9 tumors is modest in this current cohort of animals. Consistently, during the last 2 years, we

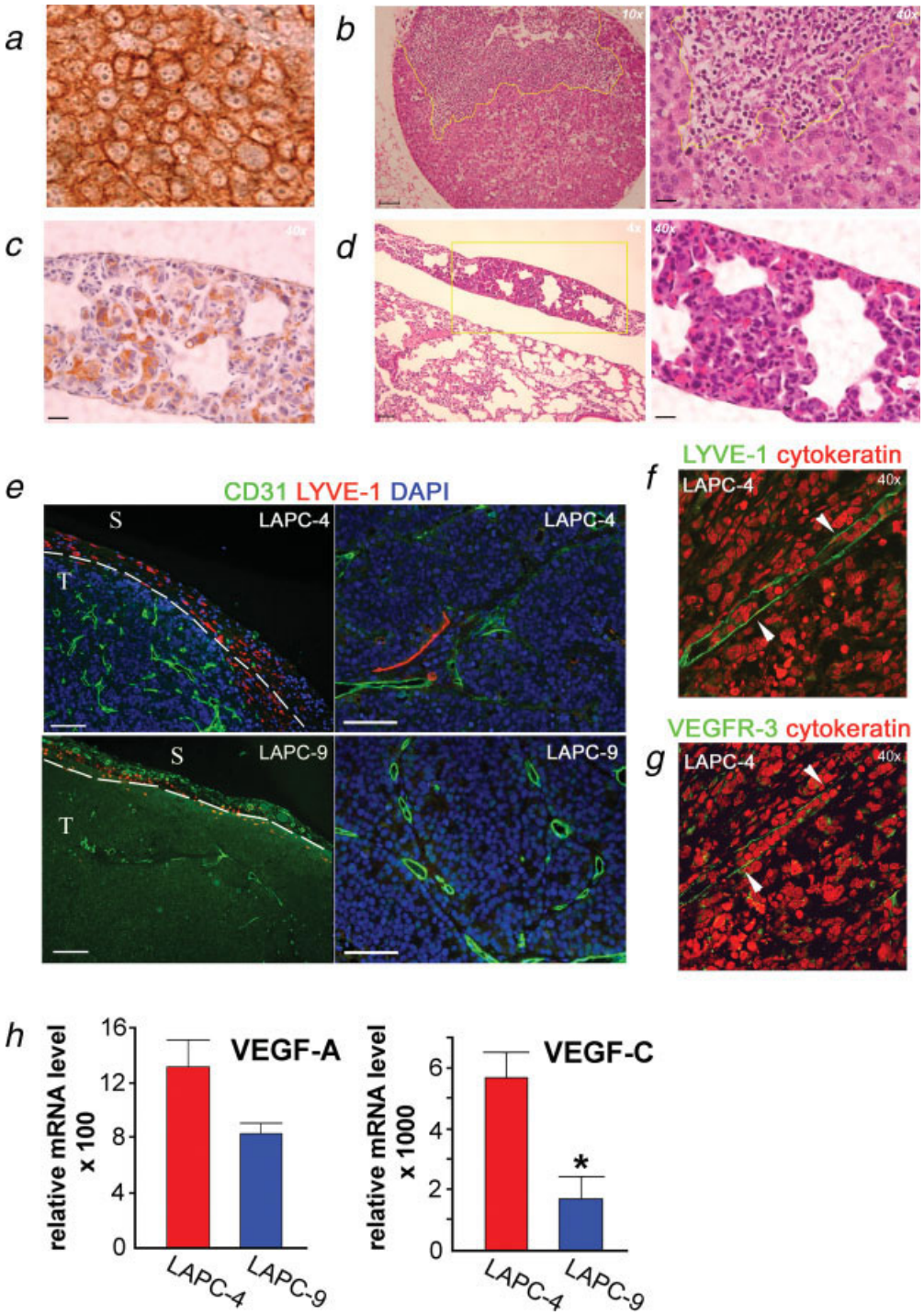

FIGURE 3 – Immunohistochemical detection of metastases and studies of angiogenic and lymphangiogenic tumor profiles. Lung and lymph node sections from LAPC-4- and LAPC-9-implanted mice were processed to detect tumor cells in the parenchyma. LAPC-4 primary tumor sections served as positive controls for human cytokeratin (*a*). Hematoxylin & eosin stained sections revealed tumor metastases in the lymph nodes (*b*) and lungs (*d*) from the LAPC-4 group. A brachial lymph node from a LAPC-4-implanted mouse shows a large subcapsular lesion (*b*). Cytokeratin staining revealed tumor cells present in lungs in the LAPC-4-implanted group (*c*). Yellow lines indicate the tumor mass. Scale bars = 200 μm (×4), 100 μm (×10) and 25 μm (×40), respectively. The blood (CD31; green) and lymph (LYVE-1; red) vessels of the primary tumors (nuclei, blue) were visualized by immunohistochemistry. Analysis of LAPC-4 tumors revealed the presence of small lymphatics both in peritumoral and intratumoral areas (*e*, left: ×10 and right: ×20; *f*, ×40). Most LAPC-9 tumors displayed only very few lymphatic vessels at the tumor periphery (*e*, left: ×10). Scale bar in *e* = 100 μm. T, tumor; S, surrounding tissue. The intratumoral LYVE-1 positive (green) structures (*f*, ×40, white arrowheads) were also positive for another lymphatic marker, VEGFR-3 (green) (*g*, ×40, white arrowheads). Angiogenic and lymphangiogenic growth factor expressions were analyzed in the excised tumors by real time RT-PCR analysis (*h*). VEGF-A levels were found to be similar whereas VEGF-C expression levels were significantly and markedly elevated in LAPC-4 as compared to LAPC-9 tumors. $*p < 0.05$.

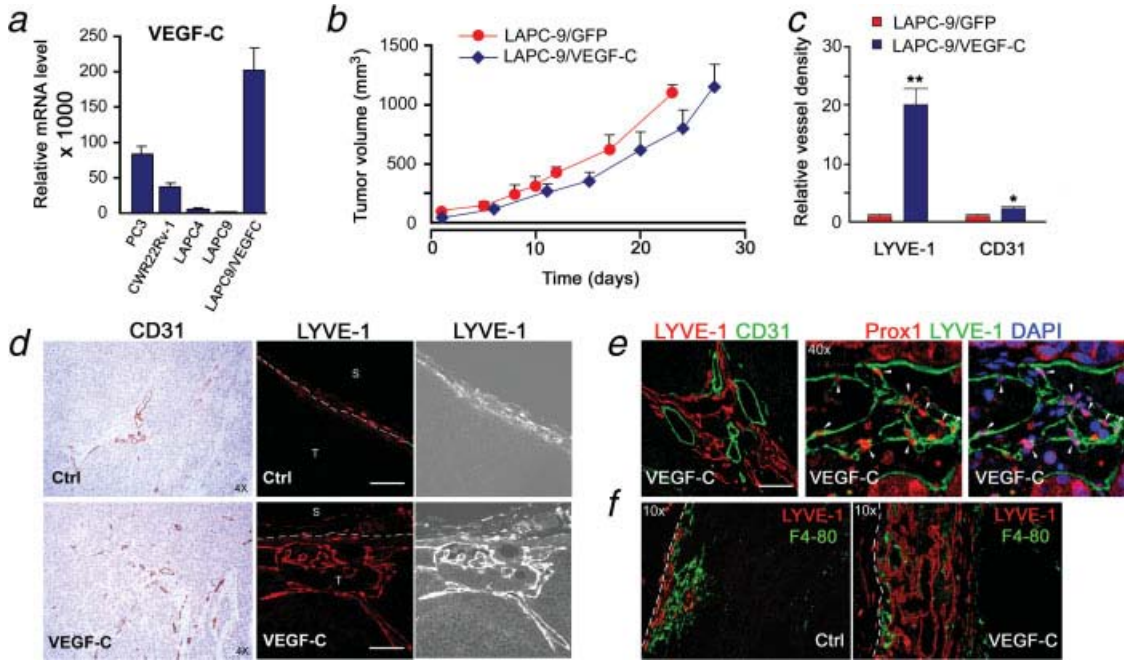

FIGURE 4 – VEGF-C expression enhances intratumoral lymphangiogenesis in LAPC-9. VEGF-C expression was determined by real time RT-PCR analysis of various prostate cancer tumor samples (*a*). Overexpression of VEGF-C in LAPC-9 results in >100-fold increase in VEGF-C levels as compared to LAPC-9/GFP tumors. This is ~ 2-fold and 4-fold higher levels as compared to PC3 and CWR22Rv-1, respectively. Primary tumor growth rates in immune-deficient mice were similar in LAPC-9/GFP- and LAPC-9/VEGF-C-implanted mice (*b*; $n = 6$–8). Tumor immunohistochemical examination revealed that blood vessels (CD31; ×4) and in particular intratumoral lymphatic vessels (LYVE-1, ×20) were more abundant in LAPC-9/VEGF-C tumors as compared to LAPC-9/GFP control tumors (*c*, *d*; S, surrounding tissue; T, tumor). Quantification analysis demonstrated that the lymphatic vessel density in LAPC-9/VEGF-C tumors (VEGF-C, blue) was 20-fold higher than in LAPC-9/GFP control tumors (Ctrl, red) (*c*; LYVE-1), whereas there was only a modest 2-fold increase in blood vessel density (*c*; CD31). Double staining for lymph (LYVE-1, red) and blood vessels (CD31, green) in LAPC-9/VEGF-C tumors revealed extensive networks of intratumoral lymph vessels growing in proximity to blood vessels (*e,* left: ×20). LYVE-1 positive structures (green) were also positive for another lymphatic marker, prox1 (red) (*e*, center and right, ×40, white arrowheads). LYVE-1 positive cells (red) did not colocalize with a macrophage marker F4/80 (green) (*f*, ×10). White scale bars in *d*, *e* = 100 μm; $*p < 0.05$, $**p < 0.005$.

have observed VEGF-C expression levels in LAPC-4 tumors ranging from 10- to 30-fold higher than in LAPC-9 tumors. This suggests that a downward drift of VEGF-C expression may be occurring in this LAPC-4 model during serial passage in scid mice.

Overexpression of VEGF-C mediates prostate cancer metastasis

To gain further insight into the role of tumor lymphatics in prostate cancer metastasis we used 2 approaches: (*i*) to examine several additional prostate cancer models as to the relation of VEGF-C expression and metastasis and (*ii*) to determine the effects of forced expression of VEGF-C in the low-metastatic LAPC-9 tumor model. The mRNA expression levels of VEGF-C were determined by quantitative RT-PCR in several prostate cancer tumor models, including CWR22Rv-1, PC3, LAPC-4, LAPC-9/GFP and VEGF-C-overexpressing LAPC-9 tumors (Fig. 4*a*). Among these, the androgen-independent, aggressive PC3 and CWR22Rv-1 tumors showed notably higher VEGF-C expression levels as compared to the androgen-dependent LAPC-4 tumors. This finding is in support of the previously published lymphatic metastatic ability of the PC3 cell line.[31] As expected, overexpression of VEGF-C in the LAPC-9 cell line using a lentiviral approach produced a robust increase in VEGF-C mRNA levels, ~2.5-fold above the level in PC3 tumors. The expression of another pro-lymphangiogenic growth factor in the VEGF family, VEGF-D, was also examined. In contrast to VEGF-C, the level of VEGF-D mRNA was negligible in all 4 prostate tumor models (data not show).

Although VEGF-C is a dominant lymphangiogenic growth factor by activating VEGFR-3,[13] it may also induce angiogenesis by binding to VEGFR-2.[32] Thus, in investigating the effects of overexpression of VEGF-C in LAPC-9 we examined the angiogenic and lymphangiogenic profiles of the tumors in detail. One million tumor cells marked with RL were implanted in the right upper back of immune-deficient mice. The LAPC-9/VEGF-C tumors showed similar *in vivo* growth rate to the LAPC-9/GFP control tumors as judged by tumor volume measurements (Fig. 4*b*) and bioluminescence signal evaluation (data not shown). The excised primary tumors were examined by immunohistochemistry to determine their vascular profiles. Intratumoral lymph vessels were much more abundant in LAPC-9/VEGF-C tumors as compared to LAPC-9/GFP control tumors that only contained few peritumoral lymphatics (Fig. 4*c*–4*f*). The overexpression of VEGF-C in LAPC-9 resulted in a slight increase in blood vessel density, whereas there was a striking 20-fold increase in intratumoral lymphatic vessel density (Fig. 4*c*). Indeed, extensive networks of intratumoral lymph vessels, consistently associated with blood vessels, were found in LAPC-9/VEGF-C tumors (Fig. 4*e*). The anti-murine LYVE-1 staining specifically identified lymphatic vessels as LYVE-1 positive structures were found to be distinct from CD31 positive blood vessels (Figs. 3*e* and 4*e*), and expressed VEGFR3 (Fig. 3*g*) as well as prox1 (Fig. 4*e*). Further, the LYVE-1 positive cells in the tumors were distinct from tumor-associated macrophages (Fig. 4*f*).

Next, several different prostate xenograft models were examined for signs of metastasis using bioluminescence imaging at the time of sacrifice. In agreement with the observed elevated expression of VEGF-C, the PC3 and CWR22Rv-1 tumor-bearing animals were found to develop prominent metastases to ipsilateral brachial and axillary lymph nodes, as well as to lung (Fig. 5*a*). In contrast, the LAPC-9/GFP-implanted control mice showed no signs of metastasis (0 out of 6). However, the induced overexpression of VEGF-C in LAPC-9 tumors was sufficient to potently

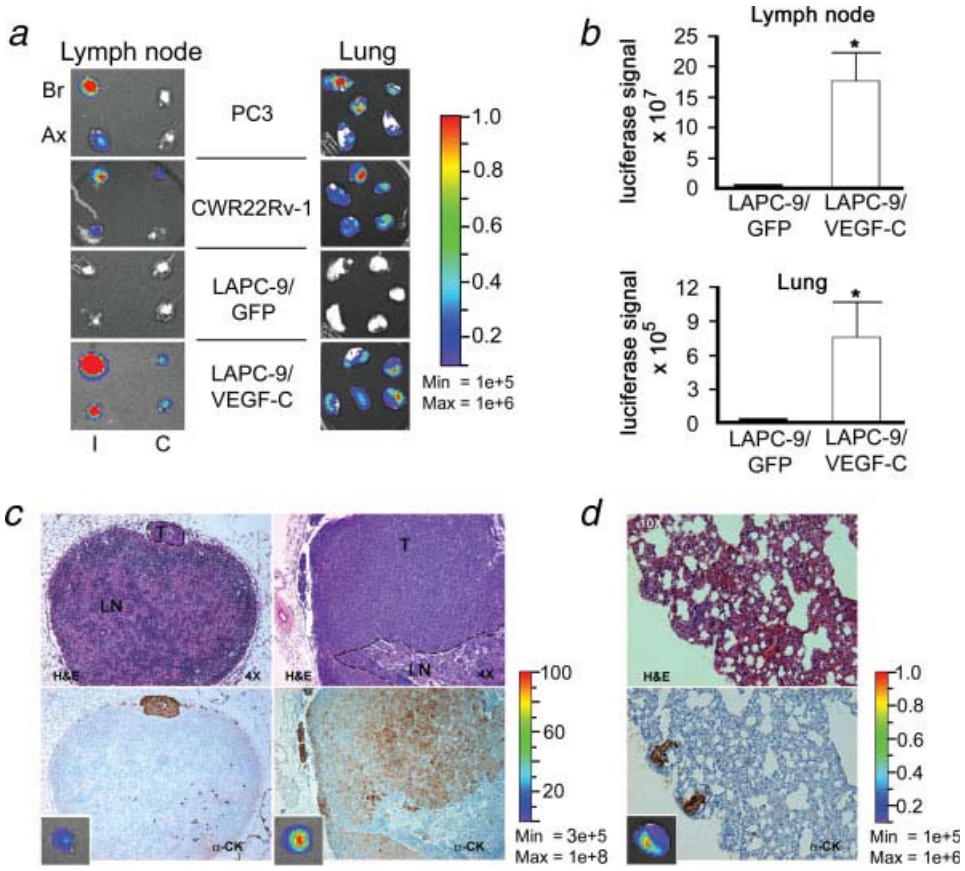

FIGURE 5 – VEGF-C expression levels correlate with development of lymph node and lung metastases. Different human prostate cancer cells were implanted in immune-deficient mice ($n = 6–8$). At sacrifice, the luciferase reporter gene (RL) activity was assayed *ex vivo* by optical imaging of dissected organs. Representative examples of bioluminescence images of lymph nodes and lungs are shown (*a*, I, ipsilateral, C, contralateral, Br, brachial lymph node, Ax, axillary lymph node). The color bars indicate the intensity range of the bioluminescence signal (p/s/cm^2/sr $\times$ 10^6). The mice bearing PC3 and CWR22Rv-1 tumors showed extensive metastasis to regional lymph nodes and lungs, whereas LAPC-9/GFP control tumors did not metastasize. Overexpression of VEGF-C in LAPC-9 resulted in intense luciferase signals in both lymph nodes and lungs, suggestive of metastasis. Quantification analysis of bioluminescence revealed that the optical signals were $\sim$ 100-fold higher in regional lymph nodes and $\sim$ 20-fold higher in lungs from LAPC-9/VEGF-C-implanted mice as compared to LAPC-9-implanted control mice (*b*). Hematoxylin & eosin (H&E, upper panel) and cytokeratin (α-CK, lower panel) staining of tissue sections confirmed the presence of tumor metastases in the lymph nodes (*c*; T, tumor; LN, lymph node, $\times$4) and lungs (*d*; $\times$10) from the LAPC-9/VEGF-C-implanted group. The corresponding whole organ optical imaging photo for each sample is shown in the small insert in the lower panels (*c*, *d*). The color bars indicate the intensity range of the bioluminescence signal (p/s/cm^2/sr $\times$ 10^6). *$p < 0.05$.

induce both lymph node and lung metastasis (Fig. 5*b*). Indeed, 63% (5 out of 8) of the LAPC-9/VEGF-C-implanted mice showed signs of lymph node metastasis, which in 60% of the mice further led to the development of lung metastases (3 out of 5). The bioluminescence intensities of the optical signals were significantly higher in regional lymph nodes and lungs from LAPC-9/VEGF-C-implanted mice as compared to LAPC-9/GFP-implanted control mice (Fig. 5*b*). These metastatic lesions in lymph nodes (Fig. 5*c*) and lungs (Fig. 5*d*) were confirmed by immunohistochemistry. Notably, the sizes of the lesions found by immunohistochemical analysis correlated with the observed bioluminescence signal intensities (Figs. 5*c* and 5*d*).

An additional role for VEGF-C in mediating metastasis has been suggested recently, where tumor cell expression of VEGFR-2 or VEGFR-3 may lead to VEGF-C-stimulated tumor cell proliferation and migration in an autocrine fashion,[33,34] resulting in enhanced tumor invasiveness and metastasis. To exclude this possibility the expression levels of VEGFR-3 in LAPC-4 and LAPC-9 tumor cells were examined by real time RT-PCR as well as by immunohistochemistry. We found that both LAPC-4 and LAPC-9 tumor cells completely lacked expression of VEGFR-3 (data not shown), indicating that the VEGF-C mediated enhancement of tumor metastasis was not due to autocrine stimulation in these models.

Discussion

Previous studies from our group have revealed the metastatic nature of LAPC-4 tumors,[22] whereas LAPC-9 tumors rarely metastasize from a subcutaneous implantation site. Hence, in our study we set forth to investigate the metastatic process and to compare the metastatic potential of these 2 models in a more quantifiable manner using molecular imaging. Findings from these recent LAPC models are likely to reflect the behaviors of slower growing, androgen-dependent prostate cancers found in the clinic. Further, we carried on to compare these LAPC models to more aggressive, androgen-independent tumors. Of note, LAPC-4 was originally derived from a regional lymph node metastase in a prostate cancer patient, whereas LAPC-9 originates from a femoral metastase.[20,24] Similarly, the PC3 cancer cell line originates from an aggressive bone metastasis, and has previously been shown in animal models to metastasize to lymph nodes, brain, lung and femurs.[31] In contrast, the CWR22 cell line originates from a nonmetastatic primary prostate cancer lesion, of which CWR22Rv-1 represent an androgen-independent xenograft subclone with capacity to metastasize mainly to lung, liver and bone in mice.[35,36]

To elucidate the underlying molecular mechanisms of metastasis, the angiogenic and lymphangiogenic profiles of these xenograft models were compared. We found that prostate cancer

metastasis correlated with the production level of lymphangiogenic growth factor VEGF-C and with tumor lymphangiogenesis. Among the 4 prostate cancer models analyzed, the 2 most aggressive, androgen-independent lines, PC3 and CWR22Rv-1, expressed the highest levels of VEGF-C and readily disseminated to regional lymph nodes and lung. The elevated VEGF-C expression of the PC3 model has previously been documented in the literature.[18,31,37] In our experience, the CWR22Rv-1 tumors exhibit abundant peritumoral and intratumoral lymphatic vessels (Burton *et al*., unpublished data). In comparing the 2 slower growing, androgen-dependent LAPC-4 and -9 models, the former was found to express elevated levels of VEGF-C concomitant with the occurrence of intratumoral lymphatics. This moderate stimulation of lymphangiogenesis was sufficient to induce tumor metastasis in all animals bearing LAPC-4 tumors, albeit with a prolonged latency of metastasis as compared to PC3 and CWR22Rv-1 models. In contrast, LAPC-9 tumors, expressing the lowest VEGF-C among the 4 models and lacking intratumoral lymphatics, did not metastasize. In further support of a predominantly lymphatic route of metastasis we found that induced overexpression of VEGF-C in the weakly metastatic LAPC-9 prostate cancer model resulted in stimulation of lymphangiogenesis leading to a highly metastatic tumor phenotype. Specifically, the fact the angiogenic profiles (*i.e.,* the degree of vascularity and the level of expression of VEGF-A between LAPC-4 and LAPC-9 tumors or between LAPC-9/VEGF-C and LAPC-9/GFP control tumors) were comparable indicates that angiogenesis is likely not the key factor accounting for the tumors differential abilities for metastatic spreading in our animal models. In contrast, the main factor seems to be molecular differences related to tumoral lymph vessels.

Our conclusion that tumoral lymphatic vessel content is the major factor accounting for the tumor's metastatic ability is supported by the following findings: (*i*) Metastases were observed in ipsilateral regional lymph nodes in the expected primary lymph drainage pathways, indicative of a lymphatic route of tumor dissemination. (*ii*) VEGF-C, a lymphangiogenic growth factor, was expressed at 3.3-fold higher levels in metastatic LAPC-4 tumors as compared to in low-metastatic LAPC-9 tumors. (*iii*) Peritumoral and especially intratumoral lymphatics were comparatively more abundant in LAPC-4 than in LAPC-9 tumors. (*iv*) Notably enlarged tumoral lymphatic networks were found after overexpression of VEGF-C in LAPC-9 tumors, resulting in a significantly increased density of intratumoral lymphatics as compared to LAPC-9 control tumors. (*v*) Overexpression of VEGF-C in LAPC-9 resulted in the development of lymph node and lung metastases. (*vi*) LAPC-4 and LAPC-9 tumor cells lacked expression of VEGFR-3 thus excluding the possibility of autocrine stimulation by VEGF-C of tumor cell invasiveness. Collectively, our findings indicate that VEGF-C-induced tumor lymphangiogenesis is sufficient to cause metastasis regionally (lymph nodes) and systemically (lungs) in low-metastatic prostate cancer models. Our data together with other studies suggest a central role for the lymphatic system in mediating prostate cancer metastasis.

Whether the prostate cancer metastasis is mediated by stimulation of intratumoral or peritumoral lymphangiogenesis or simply by activation of preexisting peritumoral lymphatics may however depend on the particular tumor aggressiveness and its microenvironment, as suggested by the differing observations obtained in experimental as well as in clinical studies.[18,38–41] For instance, a recent experimental study of the role of lymphangiogenesis and VEGF-C in prostate cancer metastasis suggested that peritumoral lymphatics, but not intratumoral lymphatics, contributed to lymph metastasis from an ortotopic site.[39] Theoretically, tumors developing *in situ* in the prostate may have immediate access to a more elaborate network of preexisting large lymphatics than tumors implanted in subcutaneous locations. Thus it is possible that while the former may achieve access to the lymphatic network by expressing lymphangiogenic growth factors that act to enlarge and dilate preexisting lymph vessels,[42] the latter may depend more on genuine stimulation of lymphangiogenesis, either in the tumor periphery or intratumorally, to establish contact with the lymphatic network and generate lymphatic metastasis.

Evidently, other differences related to the tumor or its microenvironment may also contribute to the regulation of lymphatic metastasis. Particularly, stromal cell- (*e.g*., fibroblasts, macrophages and immune cells) and extracellular matrix-derived factors in the tumor microenvironment may all contribute to tumor lymphangiogenesis, by producing pro-lymphangiogenic growth factors.[43] However, we found that the levels of tumor-associated macrophages were not significantly different between LAPC-9 control and LAPC-9/VEGF-C tumors (Fig. 4*f*), indicating that tumor VEGF-C production and lymphangiogenesis was mainly due to tumor cell-derived VEGF-C in this model.

Additionally, the precise requirement for the lymphatic system during dissemination of the tumor cells after they reach the local lymph nodes remains unclear, although several lines of evidence seem to suggest that lymphangiogenesis in the local lymph nodes may also play an important role during tumor metastasis.[44] Clearly, further studies are essential to determine the efficacy and timing of administering inhibitors of tumoral lymphangiogenesis in preventing prostate cancer metastasis, as well as to establish to what extent these treatments will be efficient to block intratumoral *versus* peritumoral lymphatic vessel-mediated tumor metastasis.

An essential component to evaluate antimetastatic therapies is to develop animal models, in which the process of tumor growth and metastasis can be effectively monitored. Whereas the ortotopic model has the great advantage of being a better model of the clinical situation, the subcutaneous implantation models allow for more straightforward surgical manipulation during tumor resection, as necessitated in our tumor models displaying a slow rate of metastasis. In this context it should be noted that surgical intervention carries a potential risk of iatrogenic tumor cell dissemination, although we consistently only have observed metastases in animals carrying LAPC-4 or LAPC9/VEGF-C tumors, and not in LAPC-9 controls, after tumor removal surgery. In our study we show that optical bioluminescence imaging as a tool to follow semiquantitatively the development over time of metastatic lesions in mice is both feasible and informative. Promisingly for the clinic, the high energy positron emission tomography (PET) modality has recently been applied successfully for noninvasive imaging of lymph node trafficking of lymphocytes,[45] and this technique may thus, in the future, be applied for *in vivo* detection of metastases in humans.

Taken together, these molecular imaging approaches should facilitate further prostate cancer studies to delineate the molecular steps involved in stimulation of lymphangiogenesis and lymphatic metastasis. An improved understanding of the complex regulation of these events may guide the development and evaluation of novel anti-lymphangiogenic agents in suppressing lymphatic and distant metastasis in prostate cancer patients.

Acknowledgements

This work is supported by NCI SPORE program P50 CA092131 (to Dr. L.W.) and the California Cancer Research Program 3NI0226 (to Dr. L.W.). Mr. J.B. is supported by UCLA RTPS Training program No. T32-GM008652 and Dr. E.B. by the Swedish Wenner-Gren Foundations. We appreciate Dr. John Colicelli (UCLA, Los Angeles, California) for providing materials for the generation of lentiviral constructs.

References

1. National Cancer Institute. Cancer Stat Facts: Surveillance, Epidemiology, and End Results (SEER) Program. Rockville, MD: NCI, 2006.
2. D'Amico AV, Whittington R, Malkowicz SB, Fondurulia J, Chen MH, Kaplan I, Beard CJ, Tomaszewski JE, Renshaw AA, Wein A, Coleman CN. Pretreatment nomogram for prostate-specific antigen recurrence after radical prostatectomy or external-beam radiation therapy for clinically localized prostate cancer. J Clin Oncol 1999;17: 168–72.

3. Stone NN, Stock RG. Laparoscopic pelvic lymph node dissection in the staging of prostate cancer. Mt Sinai J Med 1999;66:26–30.
4. Shah RB, Mehra R, Chinnaiyan AM, Shen R, Ghosh D, Zhou M, Macvicar GR, Varambally S, Harwood J, Bismar TA, Kim R, Rubin MA, et al. Androgen-independent prostate cancer is a heterogeneous group of diseases: lessons from a rapid autopsy program. Cancer Res 2004;64:9209–16.
5. Pound CR, Partin AW, Eisenberger MA, Chan DW, Pearson JD, Walsh PC. Natural history of progression after PSA elevation following radical prostatectomy. JAMA 1999;281:1591–7.
6. Roehl KA, Han M, Ramos CG, Antenor JA, Catalona WJ. Cancer progression and survival rates following anatomical radical retropubic prostatectomy in 3,478 consecutive patients: long-term results. J Urol 2004;172:910–14.
7. Hull GW, Rabbani F, Abbas F, Wheeler TM, Kattan MW, Scardino PT. Cancer control with radical prostatectomy alone in 1,000 consecutive patients. J Urol 2002;167:528–34.
8. Cheng L, Zincke H, Blute ML, Bergstralh EJ, Scherer B, Bostwick DG. Risk of prostate carcinoma death in patients with lymph node metastasis. Cancer 2001;91:66–73.
9. Skobe M, Hawighorst T, Jackson DG, Prevo R, Janes L, Velasco P, Riccardi L, Alitalo K, Claffey K, Detmar M. Induction of tumor lymphangiogenesis by VEGF-C promotes breast cancer metastasis. Nat Med 2001;7:192–8.
10. Stacker SA, Caesar C, Baldwin ME, Thornton GE, Williams RA, Prevo R, Jackson DG, Nishikawa S, Kubo H, Achen MG. VEGF-D promotes the metastatic spread of tumor cells via the lymphatics. Nat Med 2001;7:186–91.
11. Achen MG, McColl BK, Stacker SA. Focus on lymphangiogenesis in tumor metastasis. Cancer Cell 2005;7:121–7.
12. Mandriota SJ, Jussila L, Jeltsch M, Compagni A, Baetens D, Prevo R, Banerji S, Huarte J, Montesano R, Jackson DG, Orci L, Alitalo K, et al. Vascular endothelial growth factor-C-mediated lymphangiogenesis promotes tumour metastasis. Embo J 2001;20:672–82.
13. Alitalo K, Carmeliet P. Molecular mechanisms of lymphangiogenesis in health and disease. Cancer Cell 2002;1:219–27.
14. Zeng Y, Opeskin K, Baldwin ME, Horvath LG, Achen MG, Stacker SA, Sutherland RL, Williams ED. Expression of vascular endothelial growth factor receptor-3 by lymphatic endothelial cells is associated with lymph node metastasis in prostate cancer. Clin Cancer Res 2004; 10:5137–44.
15. Kaushal V, Mukunyadzi P, Dennis RA, Siegel ER, Johnson DE, Kohli M. Stage-specific characterization of the vascular endothelial growth factor axis in prostate cancer: expression of lymphangiogenic markers is associated with advanced-stage disease. Clin Cancer Res 2005;11: 584–93.
16. Zeng Y, Opeskin K, Horvath LG, Sutherland RL, Williams ED. Lymphatic vessel density and lymph node metastasis in prostate cancer. Prostate 2005;65:222–30.
17. Tsurusaki T, Kanda S, Sakai H, Kanetake H, Saito Y, Alitalo K, Koji T. Vascular endothelial growth factor-C expression in human prostatic carcinoma and its relationship to lymph node metastasis. Br J Cancer 1999;80:309–13.
18. Lin J, Lalani AS, Harding TC, Gonzalez M, Wu WW, Luan B, Tu GH, Koprivnikar K, VanRoey MJ, He Y, Alitalo K, Jooss K. Inhibition of lymphogenous metastasis using adeno-associated virus-mediated gene transfer of a soluble VEGFR-3 decoy receptor. Cancer Res 2005;65:6901–9.
19. Jiang WG, Davies G, Martin TA, Parr C, Watkins G, Mansel RE, Mason MD. The potential lymphangiogenic effects of hepatocyte growth factor/scatter factor in vitro and in vivo. Int J Mol Med 2005;16:723–8.
20. Craft N, Shostak Y, Carey M, Sawyers CL. A mechanism for hormone-independent prostate cancer through modulation of androgen receptor signaling by the HER-2/neu tyrosine kinase. Nat Med 1999; 5:280–5.
21. Craft N, Chhor C, Tran C, Belldegrun A, DeKernion J, Witte ON, Said J, Reiter RE, Sawyers CL. Evidence for clonal outgrowth of androgen-independent prostate cancer cells from androgen-dependent tumors through a two-step process. Cancer Res 1999;59:5030–6.
22. Adams JY, Johnson M, Sato M, Berger F, Gambhir SS, Carey M, Iruela-Arispe ML, Wu L. Visualization of advanced human prostate cancer lesions in living mice by a targeted gene transfer vector and optical imaging. Nat Med 2002;8:891–7.
23. Jenkins DE, Oei Y, Hornig YS, Yu SF, Dusich J, Purchio T, Contag PR. Bioluminescent imaging (BLI) to improve and refine traditional murine models of tumor growth and metastasis. Clin Exp Metastasis 2003;20:733–44.
24. Klein KA, Reiter RE, Redula J, Moradi H, Zhu XL, Brothman AR, Lamb DJ, Marcelli M, Belldegrun A, Witte ON, Sawyers CL. Progression of metastatic human prostate cancer to androgen independence in immunodeficient SCID mice. Nat Med 1997;3:402–8.
25. Morizono K, Xie Y, Ringpis GE, Johnson M, Nassanian H, Lee B, Wu L, Chen IS. Lentiviral vector retargeting to P-glycoprotein on metastatic melanoma through intravenous injection. Nat Med 2005; 11:346–52.
26. Dull T, Zufferey R, Kelly M, Mandel RJ, Nguyen M, Trono D, Naldini L. A third-generation lentivirus vector with a conditional packaging system. J Virol 1998;72:8463–71.
27. Bhaumik S, Gambhir SS. Optical imaging of Renilla luciferase reporter gene expression in living mice. Proc Natl Acad Sci USA 2002;99:377–82.
28. Brakenhielm E, Veitonmaki N, Cao R, Kihara S, Matsuzawa Y, Zhivotovsky B, Funahashi T, Cao Y. Adiponectin-induced antiangiogenesis and antitumor activity involve caspase-mediated endothelial cell apoptosis. Proc Natl Acad Sci USA 2004;101:2476–81.
29. Cao R, Brakenhielm E, Pawliuk R, Wariaro D, Post MJ, Wahlberg E, Leboulch P, Cao Y. Angiogenic synergism, vascular stability and improvement of hind-limb ischemia by a combination of PDGF-BB and FGF-2. Nat Med 2003;9:604–13.
30. Edinger M, Cao YA, Hornig YS, Jenkins DE, Verneris MR, Bachmann MH, Negrin RS, Contag CH. Advancing animal models of neoplasia through in vivo bioluminescence imaging. Eur J Cancer 2002;38:2128–36.
31. Crowley CW, Cohen RL, Lucas BK, Liu G, Shuman MA, Levinson AD. Prevention of metastasis by inhibition of the urokinase receptor. Proc Natl Acad Sci USA 1993;90:5021–5.
32. Cao Y, Linden P, Farnebo J, Cao R, Eriksson A, Kumar V, Qi JH, Claesson-Welsh L, Alitalo K. Vascular endothelial growth factor C induces angiogenesis in vivo. Proc Natl Acad Sci USA 1998;95: 14389–94.
33. Su JL, Yang PC, Shih JY, Yang CY, Wei LH, Hsieh CY, Chou CH, Jeng YM, Wang MY, Chang KJ, Hung MC, Kuo ML. The VEGF-C/Flt-4 axis promotes invasion and metastasis of cancer cells. Cancer Cell 2006;9:209–23.
34. De S, Chen J, Narizhneva NV, Heston W, Brainard J, Sage EH, Byzova TV. Molecular pathway for cancer metastasis to bone. J Biol Chem 2003;278:39044–50.
35. Sramkoski RM, Pretlow TG, II, Giaconia JM, Pretlow TP, Schwartz S, Sy MS, Marengo SR, Rhim JS, Zhang D, Jacobberger JW. A new human prostate carcinoma cell line, 22Rv1. In Vitro Cell Dev Biol Anim 1999;35:403–9.
36. Holleran JL, Miller CJ, Culp LA. Tracking micrometastasis to multiple organs with lacZ-tagged CWR22R prostate carcinoma cells. J Histochem Cytochem 2000;48:643–51.
37. Joukov V, Pajusola K, Kaipainen A, Chilov D, Lahtinen I, Kukk E, Saksela O, Kalkkinen N, Alitalo K. A novel vascular endothelial growth factor, VEGF-C, is a ligand for the Flt4 (VEGFR-3) and KDR (VEGFR-2) receptor tyrosine kinases. Embo J 1996;15:290–8.
38. Roma AA, Magi-Galluzzi C, Kral MA, Jin TT, Klein EA, Zhou M. Peritumoral lymphatic invasion is associated with regional lymph node metastases in prostate adenocarcinoma. Mod Pathol 2006;19: 392–8.
39. Wong SY, Haack H, Crowley D, Barry M, Bronson RT, Hynes RO. Tumor-secreted vascular endothelial growth factor-C is necessary for prostate cancer lymphangiogenesis, but lymphangiogenesis is unnecessary for lymph node metastasis. Cancer Res 2005;65:9789–98.
40. Trojan L, Rensch F, Voss M, Grobholz R, Weiss C, Jackson DG, Alken P, Michel MS. The role of the lymphatic system and its specific growth factor, vascular endothelial growth factor C, for lymphogenic metastasis in prostate cancer. BJU Int 2006;98:903–6.
41. Hoshida T, Isaka N, Hagendoorn J, di Tomaso E, Chen YL, Pytowski B, Fukumura D, Padera TP, Jain RK. Imaging steps of lymphatic metastasis reveals that vascular endothelial growth factor-C increases metastasis by increasing delivery of cancer cells to lymph nodes: therapeutic implications. Cancer Res 2006;66:8065–75.
42. Zeng Y, Opeskin K, Goad J, Williams ED. Tumor-induced activation of lymphatic endothelial cells via vascular endothelial growth factor receptor-2 is critical for prostate cancer lymphatic metastasis. Cancer Res 2006;66:9566–75.
43. Schoppmann SF, Birner P, Stockl J, Kalt R, Ullrich R, Caucig C, Kriehuber E, Nagy K, Alitalo K, Kerjaschki D. Tumor-associated macrophages express lymphatic endothelial growth factors and are related to peritumoral lymphangiogenesis. Am J Pathol 2002;161: 947–56.
44. Hirakawa S, Kodama S, Kunstfeld R, Kajiya K, Brown LF, Detmar M. VEGF-A induces tumor and sentinel lymph node lymphangiogenesis and promotes lymphatic metastasis. J Exp Med 2005;201:1089–99.
45. Shu CJ, Guo S, Kim YJ, Shelly SM, Nijagal A, Ray P, Gambhir SS, Radu CG, Witte ON. Visualization of a primary antitumor immune response by positron emission tomography. Proc Natl Acad Sci USA 2005;102:17412–7.

Revised 10-19-07 *Research manuscript for Nature Medicine*

Adenovirus Mediated Gene Expression Imaging to Directly Detect Sentinel Lymph Node Metastasis of Prostate Cancer

Jeremy B. Burton[1], Mai Johnson[2], Makoto Sato[2], Sok Boon S. Koh[3], David Mulholland[1], David Stout[1], Arion F. Chatziioannou[1], Michael Phelps[1], Hong Wu[1] and Lily Wu[1,2,3‡]

[1]Department Molecular and Medical Pharmacology, [2]Department of Urology, and [3]Department of Bioengineering.

Crump Institute for Molecular Imaging, and Jonsson Comprehensive Cancer Center, David Geffen School of Medicine, University of California Los Angeles

Words in abstract:	178
Words in paper:	4635 (-legend and references)
Pages:	31
Figures:	5
References:	41
Supplemental information	2 figures & 2 movies

Key words: Adenovirus; TSTA; Lymph Node; Metastasis; PET; Luciferase; gene therapy

Running title: Adenovirus mediated lymph node detection.

‡ **Requests for reprints:** Lily Wu, Department of Urology, MRL 2210, Box 951738, University of California, Los Angeles, California 90095-1738, USA. Phone (310)-825-8511; Fax (310)-206-5343 E-mail: LWu@mednet.ucla.edu

Abstract

Pelvic lymph node metastasis in prostate cancer is the most reliable indicator of poor prognosis. The accurate assessment of nodal involvement is critical to planning treatment. Yet, there is a shortage of non-invasive imaging techniques capable of visualizing nodal lesions directly. This study demonstrates the feasibility of using recombinant human adenoviral vectors to detect nodal metastases in a human prostate cancer model. This was achieved by the prostate-restricted expression of imaging reporter genes by the viral vector coupled with the innate lymphotrophic properties of adenovirus. The prostate-specific imaging vector produces bioluminescent or Positron Emission Tomography (PET) signals that correlates with the presence of metastatic lesions in the draining lymph nodes. Peritumoral injection of viral particles expressing herpes simplex virus thymidine kinase resulted in the detection of tumor cells in the sentinel lymph nodes by PET. Significantly, this approach parallels the current lymphoscintigraphy method but enables the direct PET visualization of sentinel lymph node metastases, eliminating the need for invasive lymphadenectomy. These findings may lead to more effective diagnostic and therapeutic strategies for patients with advanced stage prostate cancer.

Introduction

The pathological findings of aggressive prostate cancer has been well documented in a large series of patients having undergone prostatectomy[1,2]. Among the adverse pathologic features, the presence of pelvic lymph node metastasis is the strongest predictor of disease recurrence and progression[3,4]. For instance, the 10-year progression free survival probabilities were 79% for organ confined disease, 53% for disease with extra-prostatic extension, and only 12% for disease with lymph node metastases[1]. Therefore, methods to accurately detect lymph node metastasis in the early stages of prostate cancer would be very helpful for tumor staging and in formulating the most appropriate treatment.

Despite the importance of lymph node status on clinical management of prostate cancer, current methods to assess pelvic lymph nodes are suboptimal. At the present time, accurate lymph node staging can only be determined by pelvic lymphadenectomy[5]. Potential complications of this procedure include lymphoceles, lymphedema, venous thrombosis and pulmonary embolism, with an estimated incidence of 20%[6,7]. Conventional imaging modalities such as computed tomography (CT) and magnetic resonance imaging (MRI) are useful in evaluating anatomical abnormalities, however, neither technology can differentiate between adenopathy related to inflammation or that caused by deposition of malignant cells without coupled percutaneous biopsy[8-10]. Thus, because of low specificity, CT and MRI are of limited value in deciding therapeutic strategies[8,9]. Recently, a novel iron oxide paramagnetic nanoparticle was developed as a MRI contrast agent capable of identifying tumor-infiltrated lymph nodes in prostate cancer patients[11]. However, this technology does not identify the presence of tumor cells

directly, rather it relies upon nodal infiltration of macrophages that have engulfed the magnetic particles. Nodal regions occupied by metastatic lesions would be inaccessible to macrophages and reflected as regions devoid of signal.

Advancements in mapping the lymphatic drainage of tumor have come mainly from the melanoma and breast cancer field, where determining the sentinel lymph node (SLN) status is the standard of care[12,13]. The current method of intraoperative lymphoscintigraphy entails the use of a gamma camera to monitor the transit of a ^{99m}Tc-filtered sulfur colloid particle from the peritumoral injection site into the first draining lymph node (SLN), which is then harvested for histopathological examination[14]. The size and surface properties of colloidal particles are key determinants of a favorable lymphangiographic imaging agent[14,15]. The current colloids range in size from 50 to 200 nm[14]. Studies have implicated the ability of human adenoviral particles (serotype 5) to be effectively transported into the lymphatic circulation[16-18]. Adenovirus's size of approximately 100nm and its negatively charged capsid likely favor its entry into the lymphatics.

We have developed several prostate-specific adenoviral vectors that express imaging reporter genes under the control of a highly amplified prostate-specific PSA promoter system (TSTA)[19,20]. In the current study we investigated whether the adenovirus containing the TSTA imaging reporter could directly detect metastasis in regional lymph nodes. We demonstrate that adenoviral vectors effectively function as lymphotropic agents and are transported to regional lymph nodes to mediate gene transfer into the metastatic prostate cancer cells. Hence, following peritumoral injection of the prostate-specific vector that expresses the PET reporter gene, herpes thymidine kinase

(sr39tk)[21], we observed PET signals only in SLNs containing metastases. Such a prostate-specific gene expression imaging modality may be very helpful towards improving the clinical management of advanced stage prostate cancer.

Results

Adenovirus traffics via lymphatics to regional lymph nodes. The most definitive function of lymphatics is to collect fluid and macromolecules from interstitial spaces and transport them to regional lymph nodes. As described extensively in the rat, injection of colloids or dyes into the lymphatic-rich front footpad results in accumulation in the ipsilateral brachial and axillary nodes. To verify that adenovirus also traverse through the lymphatics via the same route, fluorescent-tagged adenoviral vector was injected in the same manner. After 24 hours the red fluorescent virus was detected by immunohistochemistry of the brachial (**Fig. 1a**) and axillary lymph nodes. The number of viral genomes transported to and retained in regional nodes in the axilla by the paw-directed injection averaged about 60,000 copies (**Fig. 1b**). Based on the injected dose of $1x10^8$ infectious units, the estimated efficiency of viral delivery was less than 0.1%. The delivery to the axillary node is about half the level of the brachial node, and no adenoviral DNA was detected in the contralateral lymph nodes within 39-cycles of PCR. We next investigated whether the virus was transported to the lymph nodes as free infectious viral particle. After the adenovirus (AdTSTA-fl, Fig. 3a) was injected into the right forepaw, the draining lymph nodes in the ipsilateral and contralateral axilla were isolated and gently disrupted to harvest the free virus. The lymph node supernatants were applied to transduce LNCaP prostate cancer cells. In concordance with the PCR distribution data (**Fig. 1b**), transduction activity (luciferase bioluminescence) was present in the ipsilateral brachial and axillary lymph node compared to uninfected control cells (**Fig. 1c**).

To explore the feasibility of the adenoviral lymphatic mapping approach in cancerous prostate glands, we examined whether virus could effectively drain to regional lymph nodes in the murine prostate Pten knockout model[22]. This Pten(-/-) model effectively recapitulates the clinical characteristics of prostate cancer progression, from preneoplastic lesions to frank carcinoma, ultimately culminating in invasive and metastatic disease[22]. The carcinomatous prostate glands from 10 weeks old Pten(-/-) mice are enlarged compared to those from wildtype littermate (**fig. 1d**). At this stage, the Pten null model displays large lymphatics within stromal regions between cancerous ductiles (**fig. 1e**). One hour after the injection of $1x10^8$ infectious units of AdTSTA-fl into each of the dorsolateral lobe of Pten (-/-) mice, the accumulation of virus within regional lymph nodes was observed (**fig. 1f, g**). Approximately $1x10^6$ adenovirus genomes were detected by real time PCR in the periaortic (PA) lumbar lymph nodes, while lesser amount of virus was detected in more distant peritoneal lymph nodes of the mesenteric (MES) and renal lymph nodes (RLR, right and RLL, left, **fig 1g**). Collectively the data demonstrate that adenovirus can function as a lymphotropic agent while retaining gene transfer activity within the targeted lymph nodes.

We surmised that macrophages would not be an effective cellular vehicle for the adenoviral vectors as the infectivity of murine macrophage/monocyte cell lines is more than 10,000 times lower than in a prostate carcinoma cell line (**supplementary Fig 1a**). Further, extensive *in vivo* applications have demonstrated the selective nature of TSTA imaging reporter vectors to express in AR/PSA-positive prostate cells and to exclude expression in cells of other tissue origin, such as macrophages and hepatocytes[19-21,23-25] (**supplementary Fig. 1b, 1c).** Moreover, TSTA vector mediated transgene (red

fluorescent protein) expression was observed only in tumor cells and not in the associated F4/80+ macrophages (**supplementary Fig. 1b**).

Lymph node metastasis model of prostate cancer. Our recent findings demonstrated that lymphangiogenic growth factor VEGF-C plays an important role in promoting lymphatic metastasis in prostate cancer xenograft models[26]. Based on our experience, the androgen-dependent, AR/PSA-positive LAPC-9 xenograft model[27] is an excellent model for this study because, upon induced expression of VEGF-C (LAPC-9/VEGF-C/GFP), these cells exhibit consistent lymphatic metastasis when implanted at the subcutaneous (**Fig. 2**) or orthotopic site (**Fig. 5**). The tumor cells, transduced with a lentivirus encoding renilla luciferase (RL) as a reporter gene (LAPC-9/VEGF-C/GFP/RL), enable non-invasive bioluminescence imaging of tumor growth (**Fig. 2a**) and sensitive quantification of nodal metastatic lesions (**Fig. 2b, c**). We also found that the volume of nodal infiltration can be adjusted with resection of the primary tumor (**Fig. 2a, d, e**). Without primary tumor resection, micrometastases in the brachial or axillary node were consistently observed when the tumors reached about 1cm in diameter at 3-4 weeks post implantation (**Fig. 2a, b**). However, if the primary tumors were surgically resected and disseminated lesions were allowed to grow for an additional 30-40 days, then large macroscopic metastatic lesions developed; ultimately infiltrating the entire lymph node (**Fig 2d, e**). This expansion of the nodal metastases can then be monitored in resected mice bearing macroscopic lymph node lesions using repetitive radionuclide PET with (18)F-3'-fluoro-3'-deoxy-L-thymidine (^{18}F-FLT, **Fig. 2d**). For example, the progression of the highly aggressive prostate carcinoma model CWR22Rv-1/VEGF-C, can be

observed by weekly PET imaging of ^{18}F-FLT following primary tumor resection (**supplementary video 1**). We found that utilization of bioluminescence and PET imaging facilitates the accurate assessment of metastatic progression. However, metabolic PET imaging with ^{18}F-FLT or ^{18}F-FDG is insensitive for the LAPC-9 and CWR22Rv-1 human prostate tumor model.

Detecting macro-metastasis in brachial and axillary lymph nodes. Despite the above noted inefficient level of vector delivery to the axillary lymph nodes by the paw-directed injection, we selected this method to demonstrate the principle of our approach for the following reasons. Firstly, the paw-directed administrations consistently drained to brachial and axillary nodes (**Fig. 1**), which were the precise dissemination sites of the subcutaneous prostate tumors implanted in the upper back. Secondly, the forepaw is at a sufficient distance from the target tissue to ensure a lymphatic route of vector distribution and to rule out random diffusion to the regional target. Thirdly, there could be accurate differentiation between luminescent signal emitted from the injection site and that emitted from the targeted lymph node metastasis. To visualize the nodal metastasis by non-invasive imaging, we employed an adenoviral vector capable of expressing imaging reporter gene at a robust level and in a prostate-specific manner[19,20] (**Fig. 3a**). The specificity of AdTSTA-fl was retained in the paw-directed injection as compared to a constitutive CMV promoter driven vector (**supplementary Fig. 1c**). The observed paw signals could be attributed to the great magnitude of extravasated vector that remained at the injection site. We tested the diagnostic capabilities of prostate-specific imaging vectors by bioluminescence imaging (**Fig. 3b**) and PET (**Fig. 3c**) in mice expected to bear

macroscopic nodal lesions (at 30 days post resection of primary LAPC-9/VEGF-C/GFP/RL tumor in the right upper back). Following paw-directed administration of AdTSTA-fl ($1x10^7$ pfu), distinct optical signal was detected in the axillary region of tumor-bearing mice but not in control animals (**Fig. 3b**). Considering that specific and precise 3-D localization of nodal metastasis will be of great clinical utility, we assessed the utility of a prostate-specific TSTA PET reporter vector (AdTSTA-sr39tk)[21] in conjunction with its tracer 9-(4-[18F]-fluoro-3-hydroxymethylbutyl) guanine (^{18}F-FHBG) for detection of nodal metastasis. Interestingly, injecting $2x10^8$ pfu of AdTSTA-sr39tk into both ipsilateral and contralateral forepaw of mice bearing palpable lymph node lesions produced a positive signal in the ipsilateral but not contralateral axilla (**Fig. 3c**). The presence of disseminated prostate tumor cells in the ipsilateral brachial lymph node of this animal was confirmed *ex vivo* by the node's enlarged size, its GFP fluorescent signal, as well as by histological identification of extensive tumor cell infiltration (**Fig. 3d, e**). The maximum diameter of the ipsilateral lymph node was determined to be 2.54-mm, which was approximately 2-3 fold larger than the nonmetastatic contralateral lymph node. Tumor cell localized expression of sr39tk was verified in the respective lymph nodes by staining with a polyclonal antibody generated against HSV-thymidine kinase (**Fig. 3e**).

Direct detection of occult lymph node metastases. Having demonstrated the ability to detect macroscopic nodal lesions, we proceeded to determine the ability of our gene expression vector to detect microscopic metastases. A cohort of 12 mice bearing LAPC-9/VEGF-C/GFP/RL tumors of 1-cm diameter on the right upper back was divided into

two subgroups that received either $1x10^8$ or $1x10^7$ pfu of AdTSTA-fl in both paws (**Fig. 4a, b**). A specific signal was generated in the ipsilateral axilla of mice that received the higher dose of vector. Conversely, insignificant background signal was displayed in both ipsilateral and contralateral side of the animals injected with the lower vector dosage (**Fig 4b**). This finding suggests that $1x10^7$ infectious units of virus are insufficient to produce an optical signal to visualize the occult metastasis.

We next investigated delivering the AdTSTA-sr39tk PET vector in a manner emulating the current clinical method of lymphoscintigraphy[28]. Following injection around the subcutaneous LAPC-9/VEGF-C/GFP/RL tumor, the viral particles would be expected to drain to the SLN and mediate gene transfer and expression in metastatic prostate tumor cells. Indeed by this methodology, robust ^{18}F-FHBG PET signals were detected in the tumor (injection site), as well as the regional draining axillary lymph node (**Fig. 4c**). The PET signal of the tumor and the anterior axillary node can be clearly distinguished by detailed sagittal and transverse tomographic views (**Fig. 4c)** and a 3-D rendered digital movie (**supplementary video 2**). Immediately following the PET/CT scan, ipsilateral and contralateral lymph nodes were removed and radioactivity was measured using a scintillation counter. The findings from the above representative case (animal M1) are shown (**Fig. 4d**). Comparison of *ex vivo* radioactive signals revealed at least 2-fold higher counts per minute/gram tissue (CPM/g) in the ipsilateral over the contralateral nodes. Moreover, the elevated radioactive tracer activity also correlated with the presence of tumor cells in the ipsilateral axillary node as verified by the detectable RL activity (**Fig. 4d**). The quantification of PET signals in all three mice showed increased tracer uptake in the ipsilateral axillary region (ROI) over the

contralateral side (**Fig. 4e**). *Ex vivo* bioluminescence signals (RL) of the isolated lymph nodes again confirmed the presence of disseminated tumor cells in all 3 animals examined (**Fig. 4f**). Taken collectively, this tumor-directed vector delivery method appeared to reach the SLN efficiently, reinforcing the potential of adenovirus to serve as a lymphotropic agent to identify the presence of sentinel lymph node metastasis.

Detection of periaortic lymph node metastasis in an orthotopic prostate xenograft model. The potential for TSTA adenoviral vector to detect pelvic lymph node metastasis was assessed in orthotopic implanted LAPC-9/VEGF-C/GFP/RL. Each lobe of a surgically exposed prostate was injected with $2.5x10^5$ tumor cells. The tumors display an extensive network of peritumoral lymphatics extending into the margin of the tumor (**Fig. 5a**). Interestingly, orthotopic implanted tumors derived from the original LAPC-9 and CWR22Rv-1 prostate cells, without forced VEGF-C expression, also display extensive peritumoral lymphatics (**supplementary Fig. 2**). However, the incidence of lymphatic metastasis in these models in less predictable than the LAPC-9/VEGF-C model. Therefore we utilized VEGF-C over-expression model to facilitate detection of metastasis.

Fifteen days following tumor implantation, mice were injected with $1x10^8$ pfu AdTSTA-fl in each footpad to query lymph nodes involved in prostate cancer metastasis (i.e. inguinal, iliac, and lumbar)[29]. Imaging of the whole animal revealed prominent renilla luciferase signal emanating from the orthotopic tumor (**Fig. 5b**). Vector directed firefly luciferase signals could identify the superficial inguinal nodes. The deeper pelvic nodes, the likely sites of lymphatic dissemination from the prostate gland, were difficult

to detect in the living animal due the photon scattering limitations of optical bioluminescence imaging. When the pelvic lymph nodes were harvested and imaged ex vivo, the periaortic lumbar lymph node from the same animal showed considerably higher firefly luciferase signal than the inguinal nodes (**Fig. 5c**). Histological examination of the periaortic node revealed a focus of subcapsular metastasis (**Fig. 5d**). As expected, this lesion expressed human cytokeratin. By sectioning through the entire lymph node, the maximum diameter of the lesion was determined to be ~250 μm. Since the lesion was observed in 20 consecutive 5-μm transverse sections, the smaller diameter of the lesion is less than 100-μm. Approximately 400 tumor cell nuclei were scored for the represented section in the largest area of the lesion. If we assume a cell is 10 μm thick, then a conservative estimate of the maximal number of tumor cells in the lesion is 4000.

Discussion

The status of LN metastasis is crucial for prostate cancer staging and treatment planning. However, the current procedures for acquiring this information are imprecise and can result in adverse side effects. A one-step, non-invasive imaging technology that could specifically visualize SLN metastasis while further offering the potential of gene therapy mediated eradication, would be of great value to the field. In the current study, we demonstrated the direct mapping of nodal metastases by a prostate-specific gene expression imaging technology. In this approach, a recombinant replication-defective adenovirus served as the vehicle to deliver the imaging reporter gene to the tumor cells. A critical component of this approach is the ability of adenoviral particle to function as a lymphotropic agent. We demonstrated that the viral vector is transported effectively as a free and infectious virus while retaining the ability to transduce resident tumor cells in the draining lymph nodes and produce detectable reporter gene expression in a prostate-restricted manner. Both large macroscopic and occult nodal lesions from subcutaneous and intra-prostatic tumor models can be visualized by this vector-mediated imaging approach. We surmised that it is the robust, yet prostate-selective expression capability of the amplified TSTA vector that enables the direct imaging of the nodal metastases[19-21,24]. In one application, tumor-directed administration of the PET reporter vector (AdTSTA-sr39tk) produced specific ^{18}F-FHBG PET signals in the involved SLNs. To our knowledge this is the first report of exploiting the lymphotropic and the selective gene expression capability of adenoviral particles to non-invasively detect nodal metastases using the clinically relevant modality of functional PET imaging.

Extensive studies demonstrate that intravenous administration of adenoviral vectors results in substantial sequestration in the liver and reticuloendothelial system[16,30]. This biodistribution pattern points to the ineffectiveness of adenovirus to target lymphatic circulation following systemic administration. On the other hand, besides the supportive data from this study, historical evidence indicates an innate affinity of adenovirus for the lymphatic system. Adenovirus can produce persistent infections in lymphoid organs such as the adenoid, from which the first adenovirus was isolated[31]. An additional advantage of adenoviral vector mediated gene transfer approach is the prospect of inducing tumoricidal activity. For example, in addition to functioning as a PET reporter gene, the sr39tk reporter gene also acts as a suicide gene in the presence of the prodrug ganciclovir[32]. In fact, we have previously employed the dual PET imaging and therapeutic function of AdTSTA-sr39tk to treat prostate tumors[24]. It is also important to note that a wide range of tissue- and tumor-specific promoters have been successfully incorporated in adenoviral vectors to target selective types of cancer[17,33]. With this issue in mind, we recently developed a TSTA vector driven by the tumor-selective Mucin-1 promoter and showed its feasibility in detecting SLN metastasis in an orthotopic breast tumor model. Hence, the adenoviral lymphangiographic imaging technology described in this study could be readily applied in other types of tumors. This could be particularly useful in melanoma and breast cancer where determination of SLN status is a critical component of clinical treatment decisions.

Several similarities and differences exist between the technology reported here and the novel LMRI technology mentioned previously[11,34]. Both technologies employ particle-based approach to query and visualize nodal infiltration non-invasively. One of

the most attractive aspects of LMRI is its confirmed diagnostic capacity to accurately assess lymph node status after intravenous administration in patients. The proposed mechanism of action for the superparamagnetic iron oxide nanoparticles entails their internalization by macrophages, which traffic to lymph nodes and registered the changes in the nodal environment. Nevertheless, as with all indirect methods used to assess lymph node metastasis, there remains the possibility that disease states could interfere with proper assessment of nodal status. By utilizing tumor specific expression, the described adenovirus mediated technique enables the direct detection and visualization of lymph node metastases.

While the issues regarding sensitivity in our system remains to be fully elucidated, the results presented (**Fig. 3c**) suggest there is the possibility of non-invasive PET visualization of metastases. Application of AdTSTA-sr39tk was able to accurately detect lymph node metastasis in a mouse bearing 2.5-mm lymph node lesions. Currently, the clinical LMRI method is capable of detection of lesions about 5- to 10-mm in diameter[11]. Furthermore, the results of tumor directed AdTSTA-sr39tk administration (Fig. 4c) suggests that this technology has the potential to directly image histologically occult metastases. At this juncture, we are actively pursuing multi-modal imaging strategies to further evaluate the potential of our targeting technology.

Recent studies by our group and others suggested that lymphatic dissemination also promotes subsequent systemic metastasis in experimental models[26,35,36,37]. Clinical experience suggests that meticulous pelvic lymph node resection not only provides diagnostic information but also has a positive impact on prolonging disease-free survival[38]. Collectively, these findings highlight the necessity for accurate non-invasive

detection of lymph node metastasis. The current cell-specific gene expression technology demonstrates the promising capability to improve the specificity of diagnostic imaging of nodal metastasis of prostate cancer. Moreover, coupling detection and suicide-gene therapy would enable not only the accurate assessment of lymph node status, but also the prospect of preventing metastatic outgrowth and systemic spread. Therefore, this study is of utmost clinical relevance and is expected to have significant influence on the development of novel diagnostic and therapeutic options for prostate cancer patients.

Methods

Adenoviral Constructs. The construction of AdTSTA-fl, AdCMV-fl, and AdTSTA-sr39tk has been described previously[19,21,25]. Virus was grown in 293 cells and purified using cesium chloride gradient and titered by plaque forming assay on 293 monolayer cells. AdTSTA-fl was labeled with succinimidyl esters amine-reactive Alexa Fluor 555 (AF555) fluorescent dye (Molecular Probes, Carlsbad, CA) according to manufacturers recommendations. Briefly, 1 ml of virus (titer = $1x10^{10}$pfu/ml) was mixed with 0.1ml of 1 M sodium bicarbonate buffer and dialyzed in PBS for 1 hr at room temperature. Reactive dye solution was then added slowly to the virus while stirring and the reaction was incubated for 1 hour at room temperature with continuous stirring. The reaction was dialyzed again in sodium bicarbonate buffer twice for 1 hour each, and the final dialysis overnight at 4°C to separate the conjugate from labeling reagent. The resulting virus was termed AF555/AdTSTA-fl. All adenovirus was stored at –80ºC prior to use.

Detection of fluorescent viral particles in lymph nodes. Mice were injected with AF555/AdTSTA-fl virus ($1x10^7$ pfu/10µl) in the forepaw. After 24 hours, axillary and brachial lymph nodes were harvested and 4µm frozen sections were mounted on glass slides. After a brief fixation with ice-cold methanol, sections were stained with DAPI (Molecular Probes, Carlsbad, CA) and examined for the presence of viral particles using a Carl Zeiss LSM 310 Laser Scanning Confocal microscope at 100x magnification.

Intra-prostatic adenovirus administration. The progression of prostate cancer in the Pten(-/-) prostate cancer mouse model has been extensively characterized and

described[22]. The prostate of ten-week old Pten (-/-) mice was exposed by making a small abdominal incision and gently exposing the seminal vesicles. The enlarged dorsolateral prostate was injected with $1x10^8$ pfu/lobe of AdTSTA-TF followed by rapid suturing of the surgical incision. After one hour mice were sacrificed and regional periaortic, renal, and mesenteric lymph nodes were dissected.

Isolation of virus particles from lymph nodes and infectivity assay. Mice (n=3) were injected in the forepaw with $1x10^8$ pfu AdTSTA-fl (20µl in PBS). Ipsilateral and contralateral lymph nodes were dissected and placed in microcentrifuge tubes with 250µl of RPMI medium without serum. Nodal capsules were disrupted by gentle agitation with a micro-pestle (Research Products International Corp, Mt. Prospect, Illinois) followed by brief vortex and centrifugation at 5,000 RPM for 5 minutes. Supernatants were removed and applied to infect $1x10^5$ LNCaP cells/well growing in a 24-well plate. After 4-days the cells were lysed and luminescence (firefly luciferase-mediated) was detected using *in vitro* bioluminescence assay according to manufacturers recommended protocol (Promega). Total protein was measured from the whole cell lysate using Coomassie Plus® protein assay (Pierce).

Real Time PCR. Mice (n=3) were injected in the forepaw with $1x10^8$ pfu AdTSTA-fl or dorsolateral prostate as described above. Ipsilateral and contralateral lymph nodes were harvested and total DNA was extracted using column purification procedure according to manufacturer suggest protocol (Dneasy Kit, Qiagen). DNA was also extracted from purified adenovirus ($1x10^8$ pfu) in the same manner in order to generate a standard curve

for accurate quantitation. Exactly 2µl of each sample or standard was amplified in triplicate using primers specific for the E2 region of adenovirus backbone DNA[16]. Reactions were run on an Opticon Monitor 2 real time PCR machine (MJ Research/Biorad, Waltham, MA) according to the following cycling conditions: 39 cycles of 95ºC/15s, 60ºC/30s and 72ºC/30s. Samples were quantified based on the values of the standard curve.

Xenograft model of lymph node metastasis. LAPC-9 xenograft was maintained by serial passage in SCID/NK$^{-/-}$ mice (Taconic). The lentiviral vectors pCCL-VEGFC-IRES-GFP and pCCL-RL (Renilla luciferase) have been previously described[26]. Briefly, freshly dissected (1-cm^2) LAPC-9 tumors were processed into single cell suspension and transduced with lentiviral vectors at multiplicity of infection (MOI) of 1 in Iscove's modified medium (IMEM) containing 8µg/ml polybrene[21]. LAPC9/VEGF-C cells ($1x10^6$) were implanted with together matrigel on the right shoulder region of SCID/NK$^{-/-}$ mice near the midline. Tumors were allowed to reach the ethical limit of 1.5 cm in diameter, at which point either tumor resection or animal euthanasia was performed. Metastasis, post tumor resection, was monitored for up to an additional 40 days using palpation, optical imaging of RL activity, and ^{18}FLT PET imaging. For the orthotopic model, 2.5 $x10^5$ LAPC9/VEGFC/GFP/RL cells/lobe were injected with matrigel into each dorsolateral lobe of surgically exposed prostates. Tumor growth was monitored by palpation and optical imaging of renilla luciferase activity.

Animal experiments using optical imaging. Mice were injected subcutaneously in the forepaw or hind paw with 20µl of adenovirus in PBS. Following injection the paws were gently massaged for 5 minutes to stimulate lymphatic uptake. Mice were imaged optically for firefly luciferase activity at 4 days following virus administration. Briefly, mice were injected with D-luciferin (150mg/kg i.p.) and imaged with the bioluminescent imager (*IVIS 100;* Xenogen, Alameda, CA) after a 20-minute incubation. Data was analyzed using IGOR-PRO Living Image® software as described previously[23].

Animal experiments using PET imaging. Mice (n=3) with macroscopic lymph node metastases were injected in the forepaw with AdTSTA-sr39tk ($2x10^8$ pfu). Mice (n=3) receiving peritumoral administration of AdTSTA-sr39tk were injected with $1x10^8$ pfu (30µl) every day for five days. Six days after the first or only injection of AdTSTA-sr39tk animals were PET imaged as described previously[24]. Briefly, animals were injected with a single bolus (~250µCi) of ^{18}F-FHBG or ^{18}F-FLT intravenously in the tail. One hour after tracer injection, mice were scanned for 10 min in a Focus 220 micro-PET scanner (Siemens Preclinical Solutions, Knoxsville, TN). PET images were created by filtered back projection at 0.4mm pixel size with 0.8 mm slice thickness. Mice were then transferred to a micro-CT scanner (MicroCAT II, Siemens Preclinical Solutions, Knoxsville, TN), and imaged over 7 min using 70 kVp, 500 ms exposures and 360º rotation to create images with 200-micron voxel size. Fused PET-CT images were created using previously described methods[39].

PET/CT analysis. PET and the CT datasets were analyzed using AMIDE software[40]. All PET data sets were converted to percent ID/gram (%ID/g) based on a phantom

calibration constant, total injected dose, decay rate for ^{18}F, and assuming 1g/ml tissue density. Regions of interest (ROI) were drawn over the site of injection, as well as on ipsilateral and contralateral axilla. The average of the maximum pixel values from representative regions was utilized to calculate the %ID/g.

Immunohistochemistry. Tissues were fixed in 3% PFA and paraffin embedded. Sections (5μm) were stained with the prostate epithelial marker (mouse α-human cytokeratin, Biogenex, San Ramon, CA) or Lyve-1 antibody (RELIATech, Braunschweig, Germany) as previously described[26]. HRP-conjugated secondary antibody to α-cytokeratin were detected using DAB substrate (Liquid DAB Substrate Pack, Biogenex). Macrophage staining was performed using rat α-mouse F4/80 antibody (Serotec, Raleigh, NC.). RFP (red fluorescent protein) was detected from paraffin embedded sections using rabbit α-RFP antibody (Rockland Immunochemicals, Inc., Gilbertsville, PA). Secondary detection of F4/80 and RFP were performed with using biotinylated α-mouse and α-rabbit IgG antibodies, respectively (Vector Laboratories, Burlingame, CA).

Rabbit anti-HSVtk antibody was a kind gift of the Dr. Margaret Black. The 3%PFA fixed, paraffin embedded tissues sections were incubated with 1:15,000 dilution of concentrated antibody overnight at 4ºC. Multilink antibody (1:20, Biogenex) was used for secondary detection.

Statistical Analysis. All error bars in graphical data represent standard error of the mean (SEM). Student's two-tailed t-test was utilized for determination of statistical relevance between groups and $P<0.05$ was considered significant.

Acknowledgement

We deeply appreciate the insightful discussions provided by Drs. Ebba Brakenhielm, Alistair Cochran, and Jean DeKernion. This work is supported by NCI SPORE program P50 CA092131, RO1 CA101904-01, and Prostate Cancer Foundation (to L.W), and 2U24 CA092865 (to AFC). J.B is supported by UCLA RTPS Training program #T32-GM008652, and Department of Defense, CDMRP 07-1-0064 (prostate cancer predoctoral training grant). We are indebted to the technical support provided by Waldemar Ladno, Judy Edwards, and Antonia Luu of Crump Institute of Molecular Imaging.

References

1. Roehl, K.A., Han, M., Ramos, C.G., Antenor, J.A. & Catalona, W.J. Cancer progression and survival rates following anatomical radical retropubic prostatectomy in 3,478 consecutive patients: long-term results. *J Urol* **172**, 910-4 (2004).
2. Epstein, J.I., Partin, A.W., Potter, S.R. & Walsh, P.C. Adenocarcinoma of the prostate invading the seminal vesicle: prognostic stratification based on pathologic parameters. *Urology* **56**, 283-8 (2000).
3. Daneshmand, S. et al. Prognosis of patients with lymph node positive prostate cancer following radical prostatectomy: long-term results. *J Urol* **172**, 2252-5 (2004).
4. Cheng, L. et al. Risk of prostate carcinoma death in patients with lymph node metastasis. *Cancer* **91**, 66-73 (2001).
5. Link, R.E. & Morton, R.A. Indications for pelvic lymphadenectomy in prostate cancer. *Urol Clin North Am* **28**, 491-8 (2001).
6. Stone, N.N., Stock, R.G. & Unger, P. Laparoscopic pelvic lymph node dissection for prostate cancer: comparison of the extended and modified techniques. *J Urol* **158**, 1891-4 (1997).
7. Heidenreich, A., Ohlmann, C.H. & Polyakov, S. Anatomical extent of pelvic lymphadenectomy in patients undergoing radical prostatectomy. *Eur Urol* **52**, 29-37 (2007).
8. Rorvik, J. & Haukaas, S. Magnetic resonance imaging of the prostate. *Curr Opin Urol* **11**, 181-8 (2001).
9. Wolf, J.S., Jr. et al. The use and accuracy of cross-sectional imaging and fine needle aspiration cytology for detection of pelvic lymph node metastases before radical prostatectomy. *J Urol* **153**, 993-9 (1995).
10. Morgan, C.L., Calkins, R.F. & Cavalcanti, E.J. Computed tomography in the evaluation, staging, and therapy of carcinoma of the bladder and prostate. *Radiology* **140**, 751-61 (1981).
11. Harisinghani, M.G. et al. Noninvasive detection of clinically occult lymph-node metastases in prostate cancer. *N Engl J Med* **348**, 2491-9 (2003).
12. Giuliano, A.E., Kirgan, D.M., Guenther, J.M. & Morton, D.L. Lymphatic mapping and sentinel lymphadenectomy for breast cancer. *Ann Surg* **220**, 391-8; discussion 398-401 (1994).
13. Morton, D.L. et al. Sentinel-node biopsy or nodal observation in melanoma. *N Engl J Med* **355**, 1307-17 (2006).
14. Szuba, A., Shin, W.S., Strauss, H.W. & Rockson, S. The third circulation: radionuclide lymphoscintigraphy in the evaluation of lymphedema. *J Nucl Med* **44**, 43-57 (2003).
15. Ikomi, F., Hanna, G.K. & Schmid-Schonbein, G.W. Size- and surface-dependent uptake of colloid particles into the lymphatic system. *Lymphology* **32**, 90-102 (1999).

16. Johnson, M., Huyn, S., Burton, J., Sato, M. & Wu, L. Differential Biodistribution of Adenoviral Vector In Vivo as Monitored by Bioluminescence Imaging and Quantitative Polymerase Chain Reaction. *Hum Gene Ther* (2006).
17. Kishimoto, H. et al. In vivo imaging of lymph node metastasis with telomerase-specific replication-selective adenovirus. *Nat Med* **12**, 1213-9 (2006).
18. Labow, D., Lee, S., Ginsberg, R.J., Crystal, R.G. & Korst, R.J. Adenovirus vector-mediated gene transfer to regional lymph nodes. *Hum Gene Ther* **11**, 759-69 (2000).
19. Sato, M. et al. Optimization of adenoviral vectors to direct highly amplified prostate-specific expression for imaging and gene therapy. *Mol Ther* **8**, 726-37 (2003).
20. Iyer, M. et al. Two-step transcriptional amplification as a method for imaging reporter gene expression using weak promoters. *Proc Natl Acad Sci U S A* **98**, 14595-600 (2001).
21. Sato, M. et al. Functionality of androgen receptor-based gene expression imaging in hormone refractory prostate cancer. *Clin Cancer Res* **11**, 3743-9 (2005).
22. Wang, S. et al. Prostate-specific deletion of the murine Pten tumor suppressor gene leads to metastatic prostate cancer. *Cancer Cell* **4**, 209-21 (2003).
23. Adams, J.Y. et al. Visualization of advanced human prostate cancer lesions in living mice by a targeted gene transfer vector and optical imaging. *Nat Med* **8**, 891-7 (2002).
24. Johnson, M. et al. Micro-PET/CT monitoring of herpes thymidine kinase suicide gene therapy in a prostate cancer xenograft: the advantage of a cell-specific transcriptional targeting approach. *Mol Imaging* **4**, 463-72 (2005).
25. Wu, L. et al. Chimeric PSA enhancers exhibit augmented activity in prostate cancer gene therapy vectors. *Gene Ther* **8**, 1416-26 (2001).
26. Brakenhielm, E. et al. Modulating metastasis by a lymphangiogenic switch in prostate cancer. *Int J Cancer* (2007).
27. Klein, K.A. et al. Progression of metastatic human prostate cancer to androgen independence in immunodeficient SCID mice. *Nat Med* **3**, 402-8 (1997).
28. Weissleder, H. & Weissleder, R. Lymphedema: evaluation of qualitative and quantitative lymphoscintigraphy in 238 patients. *Radiology* **167**, 729-35 (1988).
29. Tilney, N.L. The systemic distribution of soluble antigen injected into the footpad of the laboratory rat. *Immunology* **19**, 181-4 (1970).
30. Tao, N. et al. Sequestration of adenoviral vector by Kupffer cells leads to a nonlinear dose response of transduction in liver. *Mol Ther* **3**, 28-35 (2001).
31. Huebner, R.J., Rowe, W.P. & Chanock, R.M. Newly recognized respiratory tract viruses. *Annu Rev Microbiol* **12**, 49-76 (1958).
32. Rosenfeld, M.E. et al. Adenoviral-mediated delivery of the herpes simplex virus thymidine kinase gene selectively sensitizes human ovarian carcinoma cells to ganciclovir. *Clin Cancer Res* **1**, 1571-80 (1995).
33. Sadeghi, H. & Hitt, M.M. Transcriptionally targeted adenovirus vectors. *Curr Gene Ther* **5**, 411-27 (2005).
34. Harisinghani, M.G. et al. MR lymphangiography: imaging strategies to optimize the imaging of lymph nodes with ferumoxtran-10. *Radiographics* **24**, 867-78 (2004).

35. Roberts, N. et al. Inhibition of VEGFR-3 activation with the antagonistic antibody more potently suppresses lymph node and distant metastases than inactivation of VEGFR-2. *Cancer Res* **66**, 2650-7 (2006).
36. Cao, Y. Opinion: emerging mechanisms of tumour lymphangiogenesis and lymphatic metastasis. *Nat Rev Cancer* **5**, 725-43 (2005).
37. Lin, J. et al. Inhibition of lymphogenous metastasis using adeno-associated virus-mediated gene transfer of a soluble VEGFR-3 decoy receptor. *Cancer Res* **65**, 6901-9 (2005)
38. Bader, P., Burkhard, F.C., Markwalder, R. & Studer, U.E. Disease progression and survival of patients with positive lymph nodes after radical prostatectomy. Is there a chance of cure? *J Urol* **169**, 849-54 (2003).
39. Chow, P.L., Stout, D.B., Komisopoulou, E. & Chatziioannou, A.F. A method of image registration for small animal, multi-modality imaging. *Phys Med Biol* **51**, 379-90 (2006).
40. Loening, A.M. & Gambhir, S.S. AMIDE: a free software tool for multimodality medical image analysis. *Mol Imaging* **2**, 131-7 (2003).
41. Ray, P., De, A., Min, J.J., Tsien, R.Y. & Gambhir, S.S. Imaging tri-fusion multimodality reporter gene expression in living subjects. *Cancer Res* **64**, 1323-30 (2004).

Figure Legends

Figure 1. Adenovirus as a lymphotropic particle. a) After injection of fluorescent-labeled AF555/AdTSTA-fl ($1x10^7$ pfu, 10μl) in the paw, red fluorophore (virus conjugates, white arrows) and lymphocyte nuclei (DAPI, blue) are seen in thin sections of the brachial node at 100X amplification. **b)** To detect viral copy numbers in lymph nodes, real time PCR was performed on DNA extracted from axillary and brachial lymph nodes 24 hours after forepaw injection of $1x10^8$ pfu of AdTSTA-fl vectors. No viral DNA was detected in contralateral lymph nodes within 39 cycles of PCR. **c)** AdTSTA-fl was recovered from lymph nodes and used to infect LNCaP cells *in vitro*. Luciferase activity was measured 4 days after infection and resulting luminescence was normalized to total protein concentration, (units, RLU/s/μg protein). **d)** Gross anatomical detail of Pten(-/-) mouse prostate lobes (white arrows) shows enlargement compared to wild type littermate. **e)** Lyve-1 staining of lymphatics reveals vessels with enlarged lumens in Pten (-/-) mice compared to wild type. **f)** Anatomy of the region around the prostate shows the close proximity of the periaortic lumbar nodes (white asterisk, right-PAL; black asterisk, left-PAR). Each black box highlights the enlarged region in the subsequent photograph. **g)** Real time PCR detected viral DNA within regional lymph nodes one-hour after injection of $1x10^8$ pfu of AdTSTA-fl into each prostatic lobe (Mes, mesenteric; RLR, renal node right; RLL, renal node left) Error bars **(b,c)** are ±SEM, n=4 mice; **(c)** *Brachial, p=0.014 and *Axillary p=0.032 compared to ctrl.

Figure 2. Monitoring LN metastasis in a prostate cancer xenograft model. LAPC-9/VEGF-C/GFP/RL tumor was grafted in right upper back. **a)** The kinetics of tumor

growth can be monitored by bioluminescence imaging of renilla luciferase (RL) expressing tumor cells (scale bar represents photons/second/cm^2/steridian, (p/s/cm^2/s/sr); wk, week; dPR, days post resection). **b)** Bioluminescence (RL) in the exposed ipsilateral axillary lymph node of an animal with a tumor at week 4 (pre-resection). **c)** The corresponding subcapsular microscopic lesion is visualized by staining with hematoxylin & eosin (H&E, left) and with an antibody against human cytokeratin (brown, right). At 30 days post resection **(d)**, metastasis becomes extensive and can be detected by PET/CT imaging using ^{18}FLT (scale bar represents percent injected dose per gram, %ID/g). **(e)** Photograph (left) of this mouse with exposed right axillary node (white arrow), accessory axillary (red asterisk), and tumor regrowth (white asterisk, remaining associated with the skin). H&E staining (**e**, right) reveals extensive infiltration of tumor cells, filling the entire axillary lymph node. Inset of 20X magnification (upper left) represents the region depicted in the small box (right).

Figure 3. TSTA adenoviral-mediated detection of macroscopic lesions in lymph nodes by optical and PET imaging. **a)** A schematic representation of the TSTA adenoviral vectors used to detect nodal metastases. The binary prostate-specific TSTA expression cassette is inserted into the E1 region of the viral genome. The imaging reporter gene expressed is either firefly luciferase (fl) or an enhanced variant of herpes simplex virus thymidine kinase gene (sr39tk). **b)** Either non-tumor bearing (naïve) animal or mice at 10 days post LAPC-9/VEGF-C/GFP tumor resection (tumor-bearing) were injected with AdTSTA-fl ($1x10^7$ pfu) in the ipsilateral paw. Optical signals are seen in the axilla region of tumor-bearing mice but not in naïve animals at 4 days after viral

injection. **c)** AdTSTAsr39tk ($1x10^8$ pfu/paw) was injected in both forepaws of mice at 30 days post tumor resection. Representative coronal sections through the axilla region of a mouse are shown. Specific PET signal is detected in the ipsilateral (designated by *), but not the contralateral, axilla (scale bar in PET represents %ID/g). **d)** Dissected brachial lymph nodes from the same animal reveals gross enlargement (top) and fluorescent signal (bottom) due to the presence of GFP expressing tumor cells in the ipsilateral, but not the contralateral, lymph node. **e)** H & E staining confirmed the presence of a large tumor mass (*) within in the ipsilateral brachial node (top, left). No metastasis could be detected in the contralateral lymph node (top, right). Staining sections with HSV-tk antibody revealed strong positivity within the tumor cells of the ipsilateral lymph node (bottom, left) while contralateral control was negative (bottom, right). Black scale bar represents 20μm. Optical scale bars, $p/s/cm^2/sr$.

Figure 4. Detection of occult lymph node metastasis with bioluminescence and PET imaging. **a,b)** Early stage nodal metastasis was detected in mice bearing LAPC-9/VEGF-C/GFP tumors (s.c.) at 3 days following injection of $1x10^8$ pfu AdTSTA-fl in each forepaws. **a)** Representative image of a mouse displaying elevated optical signal was observed only in ipsilateral axilla. **b)** Quantification of firefly luciferase signal intensity in mice (n=6/group) bearing LAPC9/VEGFC/GFP tumors at ~1.0-cm diameter and injected with either $1x10^7$ or $1x10^8$ pfu of AdTSTA-fl in both forepaws. P-values are listed above bars for appropriate comparisons between groups. **c)** Representative PET images of a mouse that received tumor-directed injection of AdTSTAsr39tk ($5x10^8$ pfu in total). Sagittal and transverse PET/CT images (left) show distinctly positive PET signal

emitted from the tumor injection site (*IS*) and the draining axillary sentinel lymph node (*Ax*). To the right of each PET/CT image is the consecutive 0.4mm tomographic frames showing the PET signals through the region of interest in the right axilla; sagittal frames (A-F), transverse frames (G-L). **d)** *Ex vivo* optical (RL, p/s/cm^2/sr) and radioactive (CPM/g) signal in extracted ipsilateral (ipsi/ax) and contralateral (contra/ax) axillary lymph nodes from the mouse depicted in **(c**) reveals that the presence of tumor cells (Renilla activity) correlates with enhanced uptake of ^{18}F-HBG. **e)** Comparative ^{18}F-HBG uptake values (%ID/g) for ipsilateral and contralateral axilla in all three mice (M1, M2, M3) examined. Above each bar is the respective fold difference relative to contralateral lymph nodes. **f)** *Ex vivo* optical signal (RL) value for each axillary lymph node from the same mice in **(e)** (M1-M3). Optical values/scale bar are p/s/cm^2/sr, PET values/scale bar is percent-injected dose per gram (%ID/g).

Figure 5. Detection of occult LN metastasis in orthotopic xenograft model. a) Immunohistochemistry of LAPC-9/VEGF-C/RL orthotopic tumor displays extensive lymphatic networks (red) along the margin (dotted white line) of the tumor (tu.) extending intratumorally from the normal prostatic region (pros.). **b)** Representative optical image of RL expression (*b, left*) at 3-wks after orthotopic implantation of 2.5x10^5 LAPC9/VEGFC/GFP/RL tumor cells per lobe in the prostate of SCID/NK$^{-/-}$ mice. Injection of 1x10^8 pfu AdTSTA-fl in both hind paws of mice carrying LAPC-9/VEGF-C/RL orthotopic tumors led to observable firefly luciferase signal (*b, right*) in inguinal (Ing; left/IL, right/IR) and periaortic (PA) regions at 4 days following viral injection. **c)** *Ex vivo* firefly luciferase bioluminescence activity of dissected nodes revealed the highest

optical signal in the isolated periaortic lymph node. **d)** Histological analysis (H&E) revealed the presence of a subcapsular lesion within the periaortic lymph node at 10X magnification. This mass was verified to be LAPC9 by staining with anti-human cytokeratin antibody in a consecutive section (left, 10X).

Supplementary Figure 1. Cell specific activity of AdTSTA. a) Comparison of TSTA and CMV mediated firefly luciferase activity (RLU/s/μg protein) in prostate (LNCaP) vs. macrophage cell lines (J774 and RAW). Macrophage cell lines exhibit weak infectivity by adenoviral vectors as luciferase expression mediated by AdCMV-fl was 3-4 logs lower than in LNCaP cells. The PSA promoter-driven activity of AdTSTA-fl was clearly induced by synthetic androgen R1881 in LNCaP cells (+R1881 vs. anti-androgen Casodex, +Cas) but not in the macrophage cell lines. The prostate-specific activity of AdTSTA-fl directed a 5-6 logs higher luciferase expression in the LNCaP cells than in macrophages in the presence of R1881. **b)** Immunohistochemistry of red fluorescent protein (red), F4/80 (green) and dapi (blue) in the periphery of an adenovirus injected tumor. LAPC-9 tumor was injected with $1x10^8$ infectious units of AdTSTA-TF, expressing the triple fusion reporter gene[41]. This multifunctional reporter protein was created by fusing renilla luciferase, red fluorescence protein (RFP) and herpes thymidine kinase into a single transcriptional unit. Immunohistological staining of tumor sections, 3 days after viral injection, revealed the expression of RFP is present dominantly in tumor cells but not in the adjacent F4/80+ macrophages. **c)** *In vivo* bioluminescence at 3 days after injection of $1x10^8$ pfu AdCMV-fl or AdTSTA-fl in the left forepaw. AdCMV-fl displays high nonspecific bioluminescence signal at the site of injection (paw) and in the

liver, presumably due to redistribution from the lymphatic to the systemic circulation. In comparison to AdCMV-fl, AdTSTA-fl injection results in relatively low signal at the injection site and undetectable liver bioluminescence, indicative of the AdTSTA-fl viral particles superior tissue specificity.

Supplementary Figure 2. Lymphatics of orthotopically implanted xenografts. a) Small punctuate lymphatic vessels can be observed throughout the prostatic region associated with the LAPC-9 tumor. CWR22Rv-1 tumors, which express relatively high levels of VEGF-C, tend to have lymphatics associated with the margin and extending intratumorally. **b)** Regardless of VEGF-C expression level, orthotopic implants have peritumoral lymphatics associated with the stroma around the normal ductiles.

Supplementary Video 1. Progression of ^{18}F-FLT PET/CT detectable lymph node metastasis following resection of primary tumor, CWR22Rv-1

.

Supplementary Video 2. ^{18}F-FHBG PET/CT video of AdTSTA-sr39tk mediated visualization of sentinel lymph node metastasis.

Figure 1

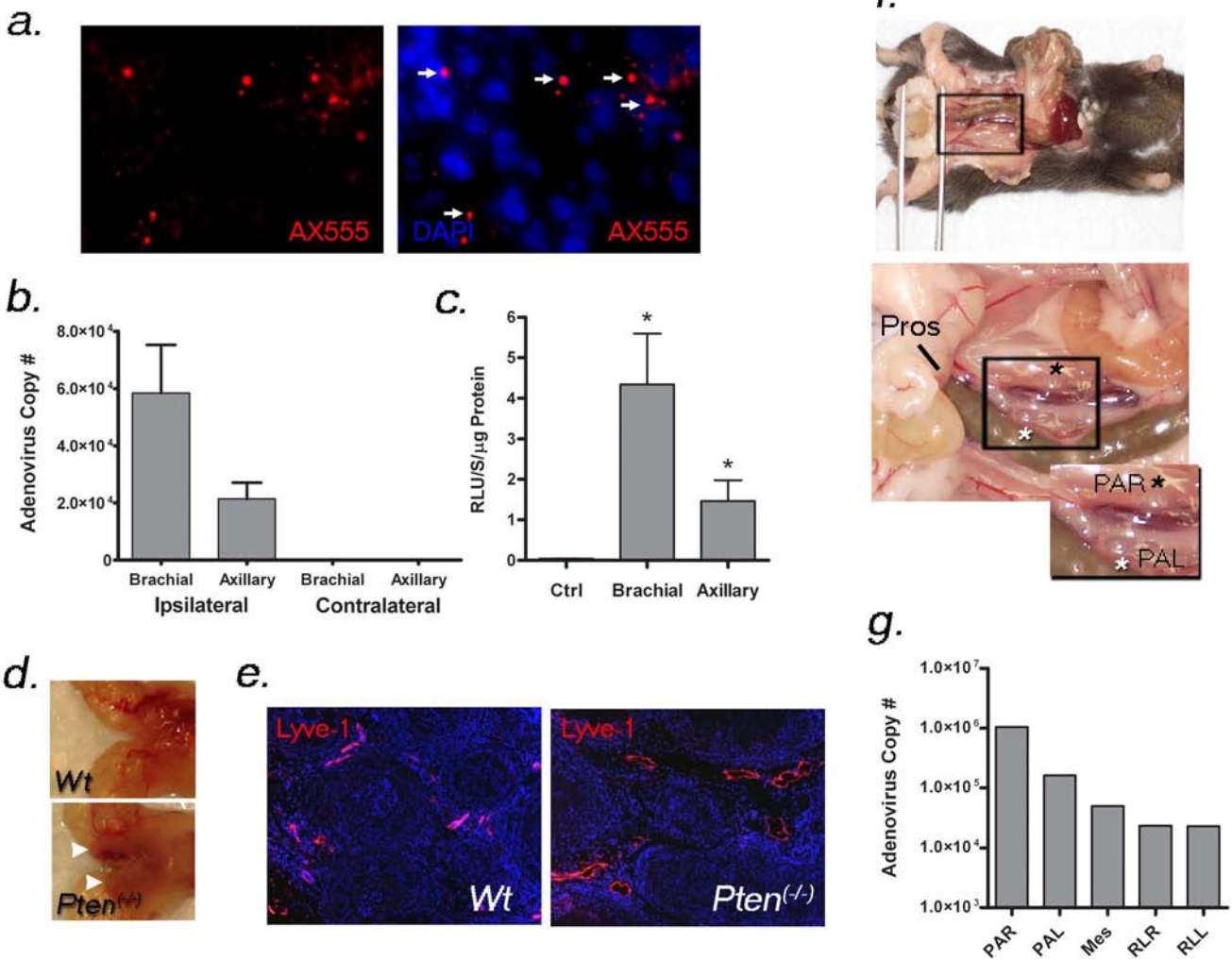
a.
AX555
DAPI
AX555
b.
Adenovirus Copy #
8.0×10^4
6.0×10^4
4.0×10^4
2.0×10^4
0
Brachial
Axillary
Brachial
Axillary
Ipsilateral
Contralateral
c.
RLU/S/μg Protein
6
5
4
3
2
1
0
*
*
Ctrl
Brachial
Axillary
d.
Wt
Pten(-/-)
e.
Lyve-1
Wt
Lyve-1
Pten(-/-)
f.
Pros
PAR
PAL
g.
Adenovirus Copy #
1.0×10^7
1.0×10^6
1.0×10^5
1.0×10^4
1.0×10^3
PAR
PAL
Mes
RLR
RLL

Figure 2

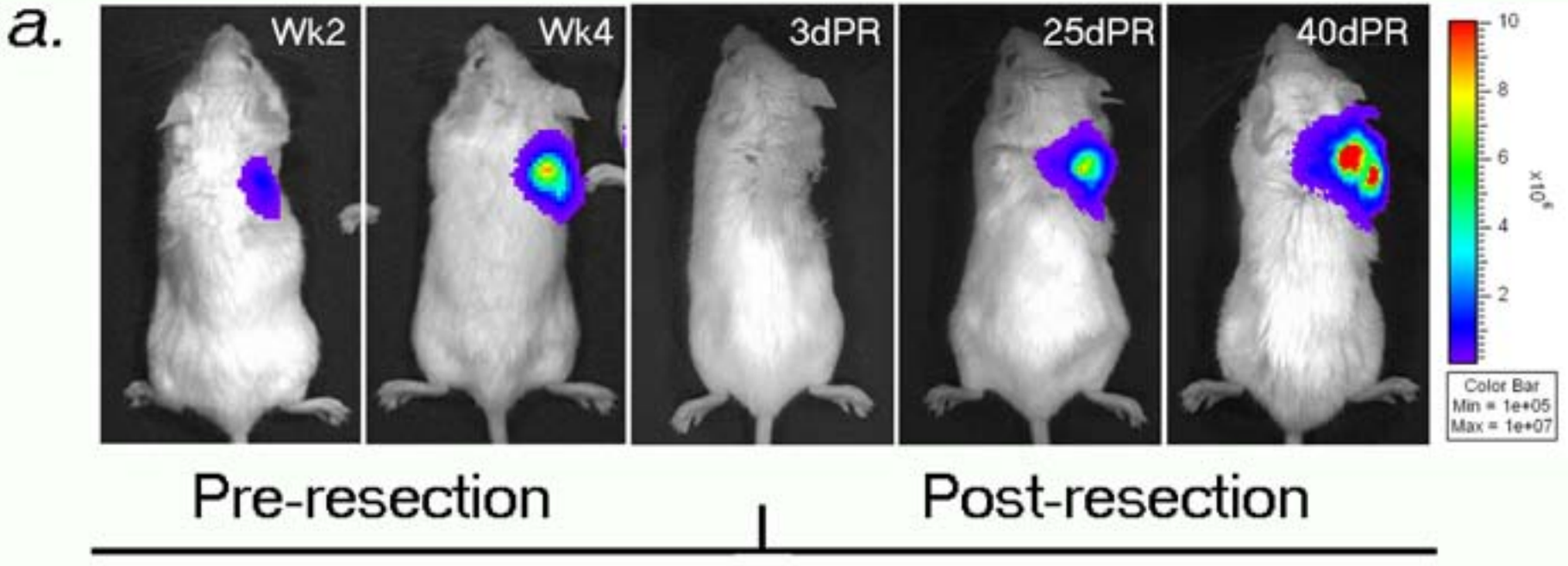
a.
Wk2
Wk4
3dPR
25dPR
40dPR
10
8
6
4
2
x10⁶
Color Bar
Min = 1e+05
Max = 1e+07
Pre-resection
Post-resection

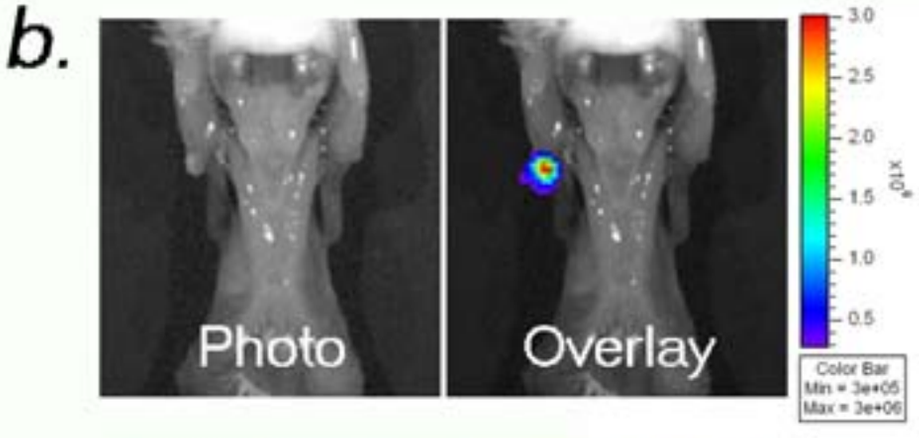
b.
Photo
Overlay
3.0
2.5
2.0
1.5
1.0
0.5
x10⁶
Color Bar
Min = 3e+05
Max = 3e+06

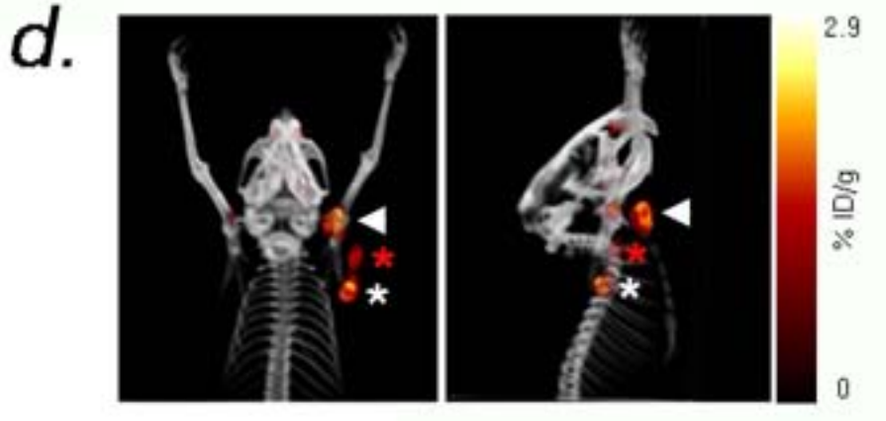
d.
2.9
% ID/g
0

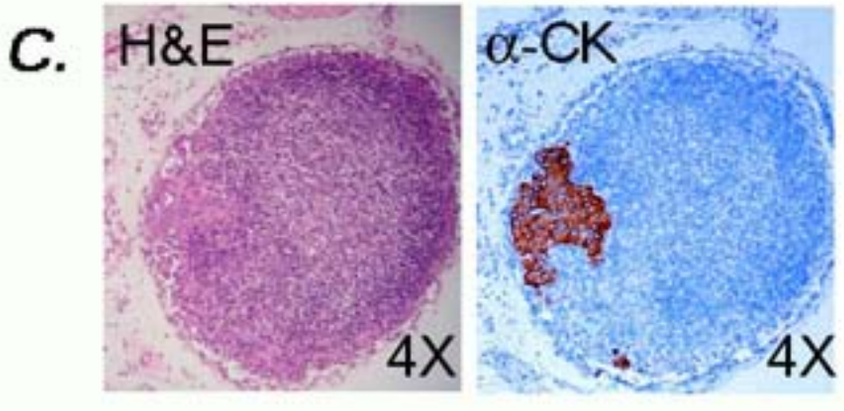
c.
H&E
4X
α-CK
4X

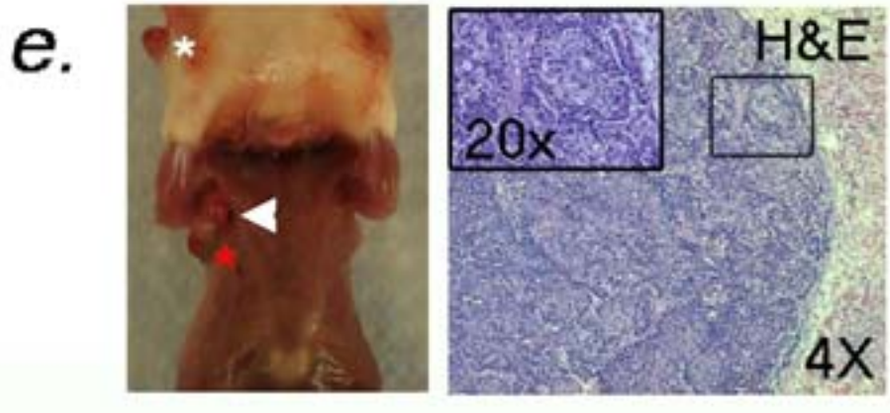
e.
20x
H&E
4X

Figure 3

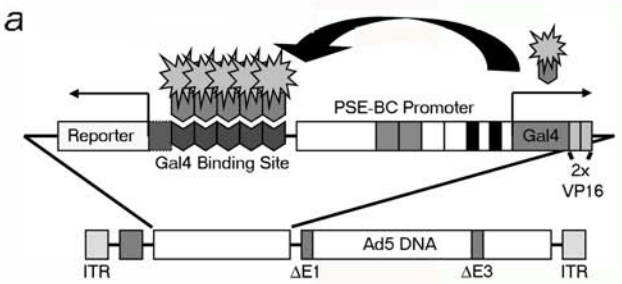
a
PSE-BC Promoter
Reporter
Gal4
Gal4 Binding Site
2x
VP16
Ad5 DNA
ITR
ΔE1
ΔE3
ITR

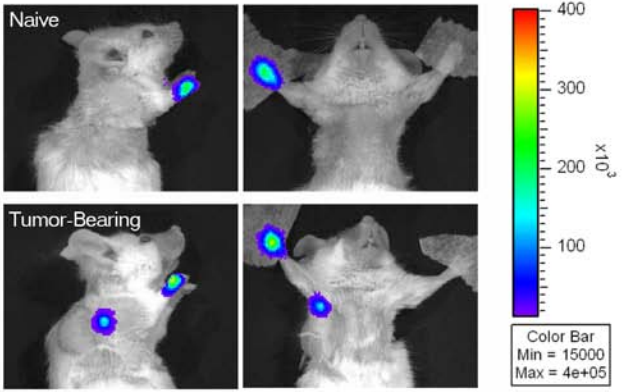
b.
Naive
Tumor-Bearing
400
300
200
100
x10^3
Color Bar
Min = 15000
Max = 4e+05

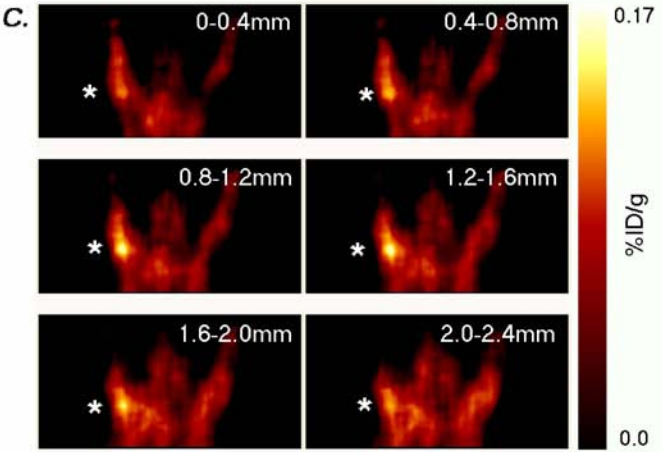
c.
0-0.4mm
0.4-0.8mm
0.8-1.2mm
1.2-1.6mm
1.6-2.0mm
2.0-2.4mm
0.17
%ID/g
0.0

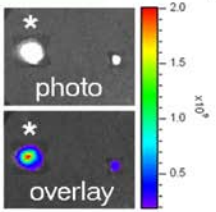
d.
photo
overlay
2.0
1.5
1.0
0.5
x10^6

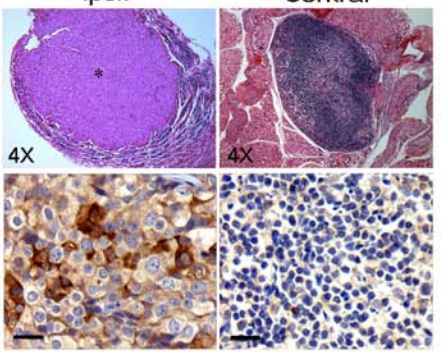
e.
Ipsi.
Contra.
H&E
4X
4X
α-HSV-tk

Figure 4

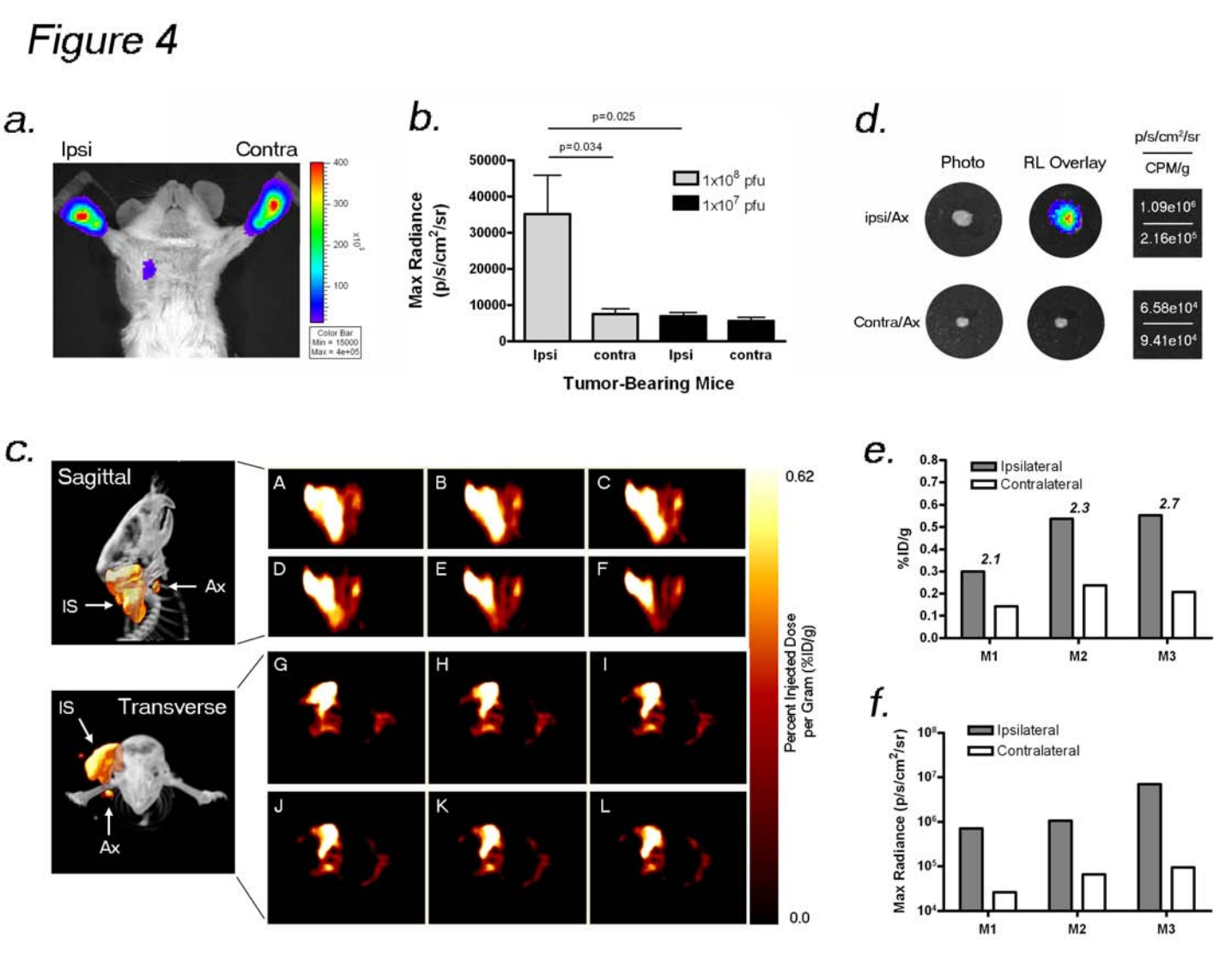
a.
Ipsi
Contra
400
300
200
100
x10³
Color Bar
Min = 15000
Max = 4e+05
b.
p=0.025
p=0.034
Max Radiance (p/s/cm²/sr)
50000
40000
30000
20000
10000
0
1x10⁸ pfu
1x10⁷ pfu
Ipsi
contra
Ipsi
contra
Tumor-Bearing Mice
d.
Photo
RL Overlay
p/s/cm²/sr
CPM/g
ipsi/Ax
1.09e10⁶
2.16e10⁵
Contra/Ax
6.58e10⁴
9.41e10⁴
c.
Sagittal
IS
Ax
Transverse
IS
Ax
A
B
C
D
E
F
G
H
I
J
K
L
0.62
Percent Injected Dose per Gram (%ID/g)
0.0
e.
Ipsilateral
Contralateral
%ID/g
0.8
0.7
0.6
0.5
0.4
0.3
0.2
0.1
0.0
2.1
2.3
2.7
M1
M2
M3
f.
Ipsilateral
Contralateral
Max Radiance (p/s/cm²/sr)
10⁸
10⁷
10⁶
10⁵
10⁴
M1
M2
M3

Figure 5

a.

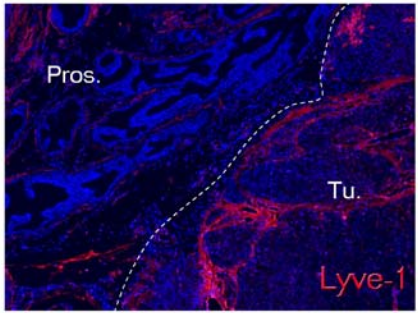

b.

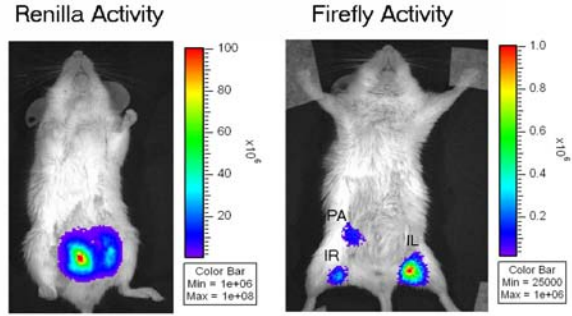

c.

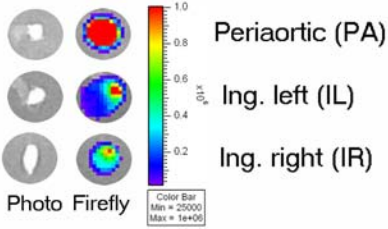

d.